



for geotechnics & structures

---

# **ENHANCED PILES/BARRETTE MODELING USING 1D ELEMENTS EMBEDDED IN 3D CONTINUUM**

## **Report 011021**

(revised 01.10.2021)

**A. Truty**

**GeoDev.**

PO Box CH-1001 Lausanne  
Switzerland  
<https://zsoil.com>



# Contents

<b>1</b>	<b>Introduction</b>	<b>5</b>
<b>2</b>	<b>Description of the approach</b>	<b>7</b>
2.1	Local embedding technique . . . . .	7
2.1.1	Pile shaft-subsoil interface . . . . .	9
2.1.2	Pile tip-subsoil interface . . . . .	12
2.1.3	Drawbacks of the local embedding method . . . . .	12
2.2	Nonlocal embedding method . . . . .	12
2.2.1	Pile shaft-subsoil interface . . . . .	14
2.2.2	Pile tip-subsoil interface . . . . .	14
2.3	Limitation of the embedding methods . . . . .	15
<b>3</b>	<b>User interface</b>	<b>17</b>
3.1	Selecting embedding method . . . . .	17
<b>4</b>	<b>Benchmarks</b>	<b>19</b>
4.1	Circular pile subject to axial loading . . . . .	19
4.2	Circular pile subject to horizontal loading . . . . .	25
4.3	Barette subject to axial loading . . . . .	35
4.4	Barette subject to horizontal loading . . . . .	41
4.5	Foundation raft . . . . .	46





# Chapter 1

## Introduction

The enhanced embedding method of 1D structural finite elements within the 3D continuum mesh enables one to analyze large scale engineering problems, like foundation rafts linked with piles/barettas, road embankments, constructed on subsoil modified by constrained modulus (CMC) or deep soil mixing (DSM) columns, any many other. The detailed FE discretization of such problems is usually very complex, may yield huge models and therefore is not practical. Moreover, each modification concerning designing piles/columns (their position and lengths) enforces new discretization of the whole computational domain. One way to overcome this serious difficulty is to work out a method that enables one to plugin a discretized pile/column/barette as a set of 1D structural elements within the 3D continuum mesh (called background mesh) at any position. It is obvious that the mesh size for the pile/column cannot be too small or too large with respect to the background mesh size. In the first case the background mesh kinematics can be overconstrained while in the latter one effects of local interaction of beam elements and the continuum will not properly be represented. In ZSoil software, till version 2020, such a method was present but its accuracy was strongly dependent on the ratio between continuum and beam elements size. In most cases when the background mesh size with respect to the column/pile diameter was within the range  $d_{col}/h^e = 1..2$  the accuracy was at the acceptable level. However in complex problems this requirement, due to constrained meshing, is usually difficult to satisfy. The main source of the problem is generated by the local form of the resulting kinematic constraints. These constraints result from interaction of 1D finite elements with 3D continuum, including skin friction and pile tip-subsoil interaction. An efficient remedy to overcome the aforementioned difficulties is to apply a certain form of non-local form of interaction between 1D finite elements and 3D continuum ones taking into account exact shape of the 1D structural element cross section. In ZSoil 2023 such an approach with low mesh dependency effects is successfully implemented. It does not include any additional data except exact shape of the 1D structural element cross section. The new approach is limited to circular and rectangular cross sections but it can easily be extended to other convex shapes.



# Chapter 2

## Description of the approach

In order to explain major differences between local and nonlocal embedding techniques the local one is presented first.

### 2.1 Local embedding technique

Let us consider the following scheme, shown in fig.(2.1), in which a set of beam elements (discretized pile or barette) are embedded within the 3D continuum. For sake of simplicity the 3D continuum is discretized using 8 node brick elements with 3 translational DOFs per node while the pile is discretized using 2 node beam elements with 3 translational and 3 rotational DOFs per node. In order to introduce Coulomb's interface between the pile and subsoil extra nodal points, occupying initially the same position as beam nodes, are added, and linked via kinematic constraints to the background mesh. In fact the two groups of interfaces are generated, the first one to represent skin friction and the second one to put an upper limit on the pile tip bearing capacity. The two extra reference tip nodes  $T_{R1}$  and  $T_{R2}$  are unified while the pile head node  $H_B$  is linked to the shell midsurface using a kinematic constraint put only on translational or, translational and rotational DOFs.

In the local embedding method a nodal vector of generalized displacements can be computed using shape functions of the background continuum element

$$\mathbf{u}(\boldsymbol{\xi}_R) = \sum_{i=1}^{nen} N_i^b(\boldsymbol{\xi}_R) \mathbf{u}_i^b \quad (2.1)$$

where  $nen$  is the number of background element nodes,  $\boldsymbol{\xi}_R$  is a vector of local (in background element frame) coordinates of a given reference node,  $N_i^b$  is the  $i$ -th background element node shape function value while  $\mathbf{u}_i^b$  is the background element  $i$ -th node vector of generalized displacements.

In order to find  $\boldsymbol{\xi}_R$  for a given nodal point within the 3D continuum element the following system of nonlinear equations has to be solved

$$\mathbf{x}_R - \sum_{i=1}^{nen} N_i^b(\boldsymbol{\xi}_R) \mathbf{x}_i^b = \mathbf{0} \quad (2.2)$$

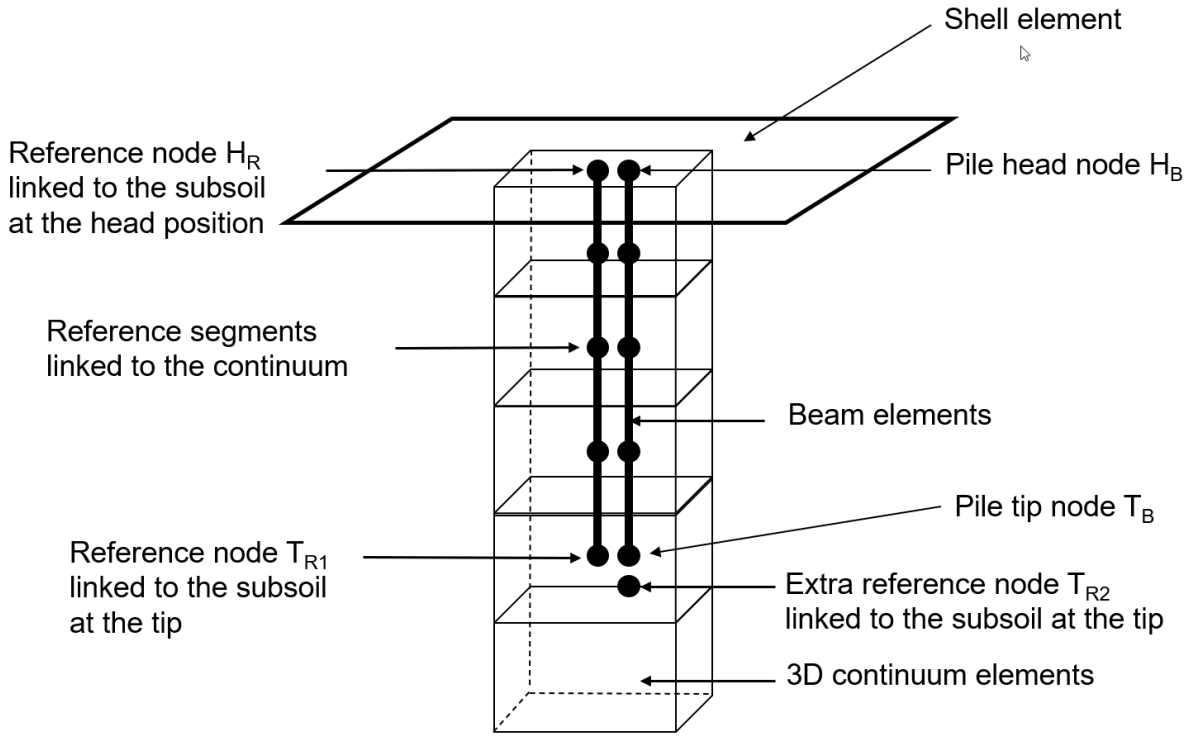


Figure 2.1: FE pile-subsoil model (beam elements embedded in 3D continuum elements)

In case when a given node has to be linked to the shell or beam element the problem must be rewritten in terms of minimizing the distance between the reference point and the axis of a beam, or midsurface of a shell element. This yields the following system of nonlinear equations to be solved

$$\left( \frac{\partial \left( \mathbf{x}_T - \sum_{i=1}^{N_{en}} N_i(\boldsymbol{\xi}_T) \mathbf{x}_i^p \right)}{\partial \boldsymbol{\xi}} \right)^T \left( \mathbf{x}_R - \sum_{i=1}^{n_{en}} N_i^b(\boldsymbol{\xi}_R) \mathbf{x}_i^b \right) = \mathbf{0} \quad (2.3)$$

To avoid penalty or Lagrange multipliers approach to satisfy eq.2.1, the reduction method of active DOFs has been adopted. This way translational DOFs of beam element nodes are not present in the linearized system of FE equilibrium equations and are expressed by translational DOFs of nodes of the corresponding background element. The penalty approach is used only to represent Coulombs interface that is put between the reference and beam nodes. In the reduction method of active DOFs some DOFs must be expressed by the other or their linear combination, as shown in eq.(2.1). Hence blocks of the resulting internal/external force vectors and stiffness matrix corresponding to the dependent node DOFs must be dispatched in a certain way onto blocks of vectors and stiffness matrix of the primary nodes. In order to understand this approach let us consider a connection between the beam element vertex A and a shell element, as shown in fig. 2.2.

The virtual work computed as  $\delta \mathbf{u}_A \mathbf{f}_A$  must be expressed using displacements of primary nodes

$$\delta \mathbf{u}_A \mathbf{f}_A = \delta \mathbf{u}_A \mathbf{k}_{AB} \mathbf{u}_B \quad (2.4)$$

where  $\mathbf{f}_A$  is an A-node block nodal force vector while  $\mathbf{k}_{AB}$  is an A-th, B-th block of a stiffness matrix of beam element. Once the DOFs of any node B in beam element are dependent on

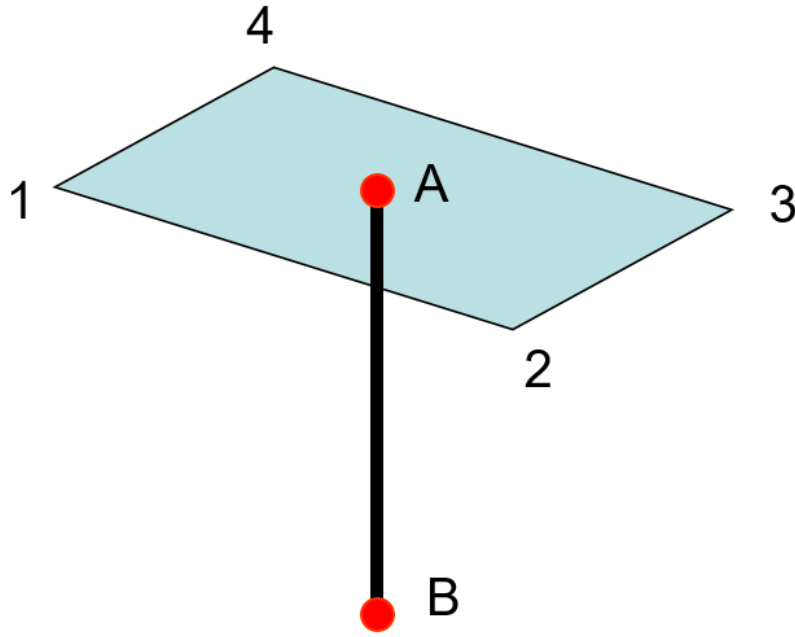


Figure 2.2: Connection of a beam element with shell at some arbitrary point

shell nodes DOFs the above expression has to be modified as follows

$$\delta \mathbf{u}_A \mathbf{f}_A = \delta \mathbf{u}_A \mathbf{k}_{AB} \mathbf{u}_B = N_i \delta \mathbf{u}_i \mathbf{k}_{AB} N_j \mathbf{u}_j \quad (2.5)$$

otherwise it takes the form

$$\delta \mathbf{u}_A \mathbf{f}_A = \delta \mathbf{u}_A \mathbf{k}_{AB} \mathbf{u}_B = N_i \delta \mathbf{u}_i \mathbf{k}_{AB} \mathbf{u}_B \quad (2.6)$$

The optimal implementation of this method should not affect standard element procedures carried out at the low level. This means that a distinct finite element should not know that its force and stiffness matrices need to be dispatched on another DOFs. Therefore dispatching procedure is run at the FE aggregation level. It is worth to mention that only some selected DOFs may be dispatched (translations for instance) not necessarily all (in case of a beam-continuum connection it is simply not possible). The resulting block structure of the dispatched stiffness matrix takes the following form

$$\mathbf{k} = \begin{bmatrix} \mathbf{k}_{11} & N_1 \mathbf{k}_{12} & N_2 \mathbf{k}_{12} & N_3 \mathbf{k}_{12} & N_4 \mathbf{k}_{12} \\ N_1 \mathbf{k}_{21} & N_1 N_1 \mathbf{k}_{22} & N_1 N_2 \mathbf{k}_{22} & N_1 N_3 \mathbf{k}_{22} & N_1 N_4 \mathbf{k}_{22} \\ N_2 \mathbf{k}_{21} & N_2 N_1 \mathbf{k}_{22} & N_2 N_2 \mathbf{k}_{22} & N_2 N_3 \mathbf{k}_{22} & N_2 N_4 \mathbf{k}_{22} \\ N_3 \mathbf{k}_{21} & N_3 N_1 \mathbf{k}_{22} & N_3 N_2 \mathbf{k}_{22} & N_3 N_3 \mathbf{k}_{22} & N_3 N_4 \mathbf{k}_{22} \\ N_4 \mathbf{k}_{21} & N_4 N_1 \mathbf{k}_{22} & N_4 N_2 \mathbf{k}_{22} & N_4 N_3 \mathbf{k}_{22} & N_4 N_4 \mathbf{k}_{22} \end{bmatrix} \quad (2.7)$$

where  $\mathbf{k}_{AB}$  is a block of the beam stiffness matrix.

### 2.1.1 Pile shaft-subsoil interface

A segment-to-segment interface element enables one to describe strong tangential displacement discontinuity between the pile and subsoil (along direction  $x_L$  (see fig.(2.3)). In any

other direction ( $y_L$  or  $z_L$ ) displacement compatibility is enforced. The local frame of this interface element is shown in the fig.(2.3).

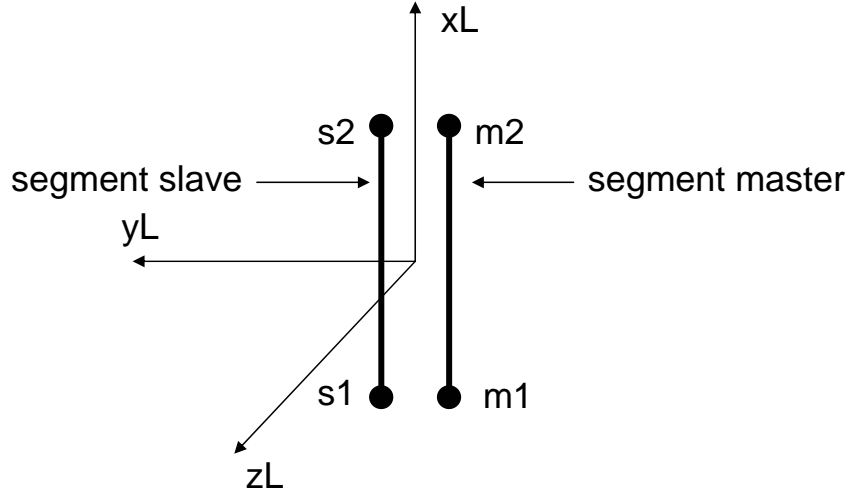


Figure 2.3: Local coordinate system of interface element

At any time instance  $t_{N+1}$  relation between trial tangential stress and tangential relative displacement can be written in the following manner

$$\tau_{N+1} = \tau_N + k_s \Delta\gamma_{N+1} \quad (2.8)$$

The true tangential stress must satisfy Coulomb's friction law

$$\|\tau_{N+1}\| \leq \sigma'_n \tan(\phi) + c \quad (2.9)$$

The increment of the relative tangential displacement is computed using the formula

$$\Delta\gamma_{N+1} = \mathbf{e}_{\mathbf{x}_L}^T (\Delta\mathbf{u}_{N+1}^s - \Delta\mathbf{u}_{N+1}^m) \quad (2.10)$$

As the cross section is not represented in the discretized model hence it is not possible to compute directly  $\sigma'_n$  required in the Coulomb's law. To bypass this serious drawback the equivalent normal effective stress in the shaft interface  $\sigma'_n$  is recovered from the continuum element in which given interface node is embedded. The equivalent normal stress value is a weighted average of normal stress values computed along the circular pile cross section as shown in the fig.(2.4).

$$\sigma'_n = \frac{\int_0^{2\pi} \min(\sigma'_n(\alpha), 0) R d\alpha}{\int_0^{2\pi} R d\alpha} \quad (2.11)$$

In the adopted method  $N = 16$  auxiliary points  $P_i$  located on the pile circuit are generated, and then for each generated point a local cylindrical frame is defined ( $x_L - y_L - z_L$ ) (axis

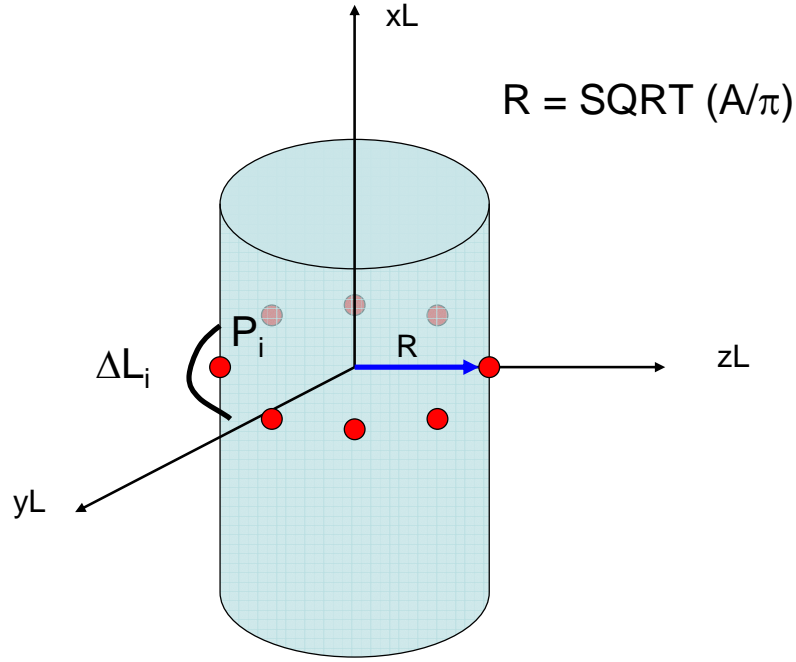


Figure 2.4: Scheme for evaluation of equivalent normal effective stress

$x_L$  coincides with the pile axis while axis  $y_L$  is the radial axis). The effective stress state is transformed then to this local coordinate system yielding the  $\sigma'_n(\alpha)$  value.

As in the shaft interface element nodal integration is used hence nodal vector of internal forces computed in the local frame (at node  $i$ ) is expressed by the formula

$$f_{x,i}^L = \frac{1}{2} L \tau_i 2\pi R \quad (2.12)$$

and  $R$  is the pile radius.

The two remaining force vector components correspond to the two kinematic constraints

$$u_{y_L}^m = u_{y_L}^s \quad (2.13)$$

$$u_{z_L}^m = u_{z_L}^s \quad (2.14)$$

and are computed using penalty method ( $k_n$  is a penalty value)

$$f_{y_L,i} = \frac{1}{2} L \sigma_{y_L,i} \quad (2.15)$$

$$f_{z_L,i} = \frac{1}{2} L \sigma_{z_L,i} \quad (2.16)$$

where

$$\sigma_{y_L,i} = k_n \varepsilon_{y_L}^i \quad (2.17)$$

$$\sigma_{z_L,i} = k_n \varepsilon_{z_L}^i \quad (2.18)$$

$$\varepsilon_{y_L} = \mathbf{e}_{y_L}^\top (\mathbf{u}^s - \mathbf{u}^m) \quad (2.19)$$

$$\varepsilon_{z_L} = \mathbf{e}_{z_L}^\top (\mathbf{u}^s - \mathbf{u}^m) \quad (2.20)$$

### 2.1.2 Pile tip-subsoil interface

In order to be able to analyze the pull-out test and to reduce potential excessive normal force transferred through the pile tip an extra node-to-node interface is added with the local frame inherited from the pile (local axis  $x_L$  coincides with the pile axis and is directed downwards in this case).

The normal stress component (along  $x_L$  axis) of the internal force vector is computed as follows

$$f_{x_L} = \sigma_n \pi R^2 \quad (2.21)$$

$$\sigma_n = k_n \varepsilon_n \quad (2.22)$$

$$\varepsilon_n = \mathbf{e}_{x_L}^\top (\mathbf{u}_{T_{RB}} - \mathbf{u}_{T_B}) \quad (2.23)$$

The resulting normal stress  $\sigma_n$  is limited by the two inequalities

$$0 \geq \sigma_n \geq -q_c \quad (2.24)$$

### 2.1.3 Drawbacks of the local embedding method

The local embedding method may be highly sensitive to the background mesh density in case when background elements are relatively small with respect to the pile diameter. Therefore it is very important to enforce background grid size of order of one to two pile diameters.

## 2.2 Nonlocal embedding method

In order to eliminate strong impact of the background mesh size on the resulting deformations and stress resultants in the embedded beam elements a method of non-local kinematic constraints has been adopted here. To explain this new method let us consider segment of a pile embedded in the 3D continuum as shown in the fig.2.5.

In order to dispatch beam stiffness matrix and force vector on the background 3D continuum mesh, taking into account real dimensions of the pile cross section, an extra grid is generated with the control points located at grid cell centers. It is obvious that for the circular cross section some of these cells are not filled by the pile cross section and some of them are fully or partially filled. This way each control point has an associated weight equal to the fraction of the filled grid cell area to the total pile cross section. The necessary condition is such that sum of these weights must be equal to one. In case of the rectangular cross section



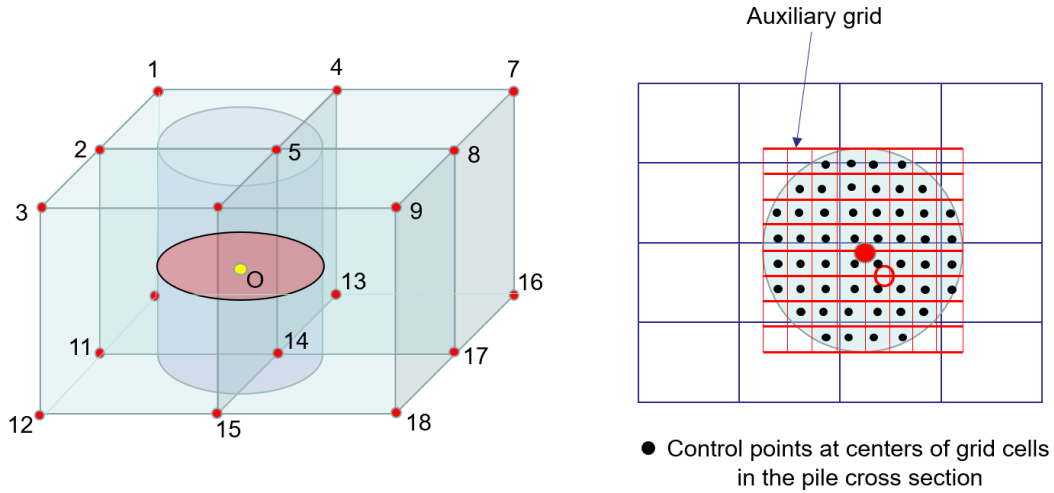


Figure 2.5: Pile segment as a beam element embedded in the 3D continuum mesh (left figure); superposed auxiliary grid cells and 3D mesh

(barette) the problem is much simpler as all weights are equal. In the non-local embedding method displacement vector corresponding to node O will depend on displacement vectors of all nodes of a set of 3D continuum elements in which at least one control point is located. If we consider the above example (see fig.2.5) displacement vector of node O will depend on displacement vectors of 18 nodal points and not just 8 as in the local version. For denser background 3D continuum meshes number of contributing nodal points can be much larger. The procedure used to compute dispatch node weights is given in Box.2.1. Note that notion of dynamic data collections like sets and dictionaries (or maps in C++) is used for robust implementation.

#### Box.2.1 Computing dispatch node weights

1. For given: set of cross section control points  $\{A_k\}$  and control points weights  $\{w_{A,k}\}$
2. Create an empty dictionary of dispatch nodes weights  $\{w_{N,m}\} = \{\}$  in which dispatch node global number is the key
3. Loop over each control point  $A_k$ 
  - find embedding element and vector of local coordinates  $\xi_k$  of control point  $A_k$
  - compute standard shape functions  $\mathbf{N}(\xi_k)$  for the embedding element
  - Loop over embedding element nodes  $i = 1..n_{en}$ 
    - ★ get global number of the element node  $i$
    - ★ if the global node number does not appear in dictionary  $\{w_{N,m}\}$  keys then add it to the dictionary with the current dispatch node weight equal to  $N_i w_{A,k}$
    - ★ if the global node number appears already in dictionary  $\{w_{N,m}\}$  keys then add  $N_i w_{A,k}$  to the current dispatch node weight
4. Normalize dispatch node weights

## 2.2.1 Pile shaft-subsoil interface

Modeling skin friction in the non-local embedding method is different from the one used in the local one. First of all in the 1D segment-to-segment interface element one segment coincides with the beam element while the second segment is linked to the background 3D mesh using non-local kinematic constraint. Another difference is such that due to nonuniform normal stress distribution in the circumferential direction (this may happen for non-axial loading conditions) the resulting shear force is integrated from tangential stresses computed at stress control points located along pile/barette circuit (see fig.2.6). To enable this action each stress control point is located in the background 3D continuum mesh and current stress state is set using superconvergent patch recovery method. Once the stress state is defined at the control point the normal effective stress component is computed using standard tensorial transformation rule.

### Box.2.2 Integrating tangential force component

1. For given accumulated increment of the tangential displacement (at time step  $N+1$ )  $\Delta\gamma_{N+1}$  perform
  - Nullify tangential force value  $f_{s,N+1} = 0$
  - Loop over stress control points  $S_i, \quad i = 1..N_\sigma$
  - Using effective stresses from the previous iteration run super-convergent patch recovery procedure to obtain effective stress state at the stress control point embedded in the 3D continuum  $\rightarrow \sigma_i$
  - Form local frame in which first axis coincides with the pile axis, the second coincides with the external normal to the pile/barette cross section circuit and the 3-rd one is a cross product of the first two, then set transformation matrix  $\mathbf{T}$
  - Compute normal stress component (22 component in the local frame)  $\sigma_n = \sigma_{22} = T_{2k}T_{2r}\sigma_{kr}, \quad k = 1..3, r = 1..3$
  - Compute trial tangential stress  $\tau_{i,N+1}^{\text{trial}} = \tau_{i,N} + k_t \Delta\gamma_{N+1}$
  - If  $\sigma_n > 0$  then separation condition is detected, assume  $\tau_{i,N+1} = 0$
  - If  $\sigma_n \leq 0$  and  $\|\tau_{i,N+1}^{\text{trial}}\| + \sigma_n \tan \phi - c \leq 0$  then stick condition is detected hence  $\tau_{i,N+1} = \tau_{i,N+1}^{\text{trial}}$
  - If  $\sigma_n \leq 0$  and  $\|\tau_{i,N+1}^{\text{trial}}\| + \sigma_n \tan \phi - c > 0$  then slip condition is detected hence  $\tau_{i,N+1} = \text{sign}(\tau_{i,N+1}^{\text{trial}}) (-\sigma_n \tan \phi + c)$
  - Integrate tangential force  $f_{s,N+1} = f_{s,N+1} + \tau_{i,N+1} \Delta s \frac{1}{2} L$

## 2.2.2 Pile tip-subsoil interface

Modeling pile tip-subsoil interaction in the non-local embedding method is very similar to the local version with the only difference such that the reference node displacement vector is set up using non-local constraint.

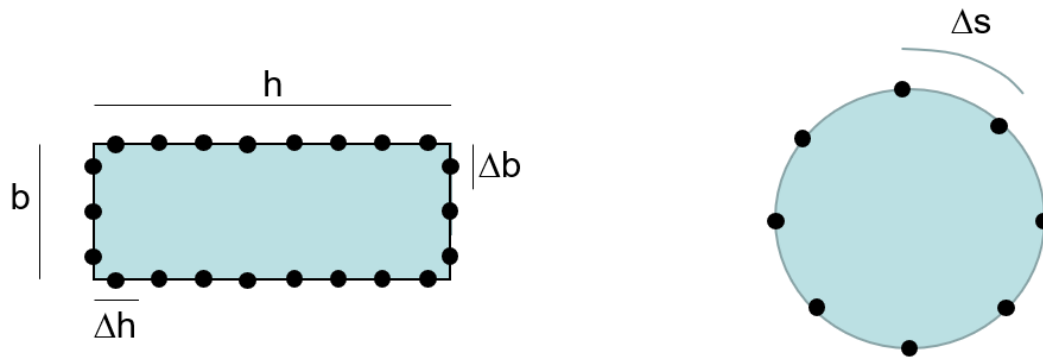


Figure 2.6: Location of stress control points for different 1D insert cross sections

## 2.3 Limitation of the embedding methods

**In the current implementation piles/baretttes cannot be located at symmetry planes, no matter if the local or non-local embedding method is used.**



# Chapter 3

## User interface

### 3.1 Selecting embedding method

The user interface to set up piles/baretttes is practically the same as in previous ZSoil versions except the additional check-box which enables one to switch between local/nonlocal embedding methods. This is the only difference between the new ZSoil 2023 and older versions as far as simplified piles modeling is concerned. **Note that baretttes can only be analyzed using nonlocal embedding method.**

Pile setup

Beam director

☒ By vectors ☐ By points

X: 1 X: 1  
Y: 0 Y: 0  
Z: -0 Z: -0

Node 1 [m] Node 2 [m]

X: 0 X: 0  
Y: 0 Y: -8  
Z: 0 Z: 0

☒ Create pile-soil interface  
☐ Create pile tip-soil interface  
☒ Full sticking at pile tip-soil interface

☒ Nonlocal interaction for pile head, tip and shaft

Pile head linking

☐ Link pile head [dropdown]  
☒ Translational DOFs  
☐ Rotational DOFs

Parameters

Pile material : 4 4: No name  
Pile-soil interface material : 5 5: No name  
Pile tip-soil interface material : 0 <Edit...>  
Existence function : 2 2: No name

Split

☐ Number of segments 10  
☐ Segment length 1 [m]  
☐ Automatic (equal split)  
☒ Automatic (adaptive spl)  
Eliminate segments shorter than 0.25 [m]

OK Cancel

Local-nonlocal embedding switch

Figure 3.1: User interface to set up piles/baretttes with local/nonlocal embedding switch



# Chapter 4

## Benchmarks

### 4.1 Circular pile subject to axial loading

Input files:

pile-axial-3D-cont-frict.inp,  
pile-axial-embb-mesh-as-3D-frict.inp,  
pile-axial-3D-cont-frict-with-tip-cnt-ex.inp,  
pile-axial-embb-mesh-80cm-frict.inp,  
pile-axial-embb-mesh-120cm-frict.inp,  
pile-axial-embb-mesh-80cm-tip-refined-frict.inp,  
pile-axial-embb-mesh-120cm-tip-refined-frict.inp

In this section an axial load test carried out on the 8m long circular pile ( $\phi = 80\text{cm}$ ) is analyzed. The reference 3D model is discretized using 8 node brick elements. Subsoil is modeled using perfect elasto-plastic Mohr-Coulomb model. Material properties used in this benchmark are summarized in tables 4.1 and 4.2.

Results of the reference model are then compared with the results of simplified models in which the pile is treated as a set of beam elements embedded in the 3D continuum using non-local embedding method.

The 3D mesh of the reference model is shown in the fig.4.1. Two contact interface setups are considered, the one with the skin interface only and the second one with additional interface at the pile tip but also extra interfaces in the zone of the skin-pile tip surfaces intersection (see fig.??).

The simplified method is verified using three different meshes. In the first simplified model the background mesh is equivalent to the mesh of the full 3D reference model (see fig.4.3). In the next two simplified models uniform structured 3D meshes with the uniform grid size (in X-Z plane) 80cm and 120cm are used (see fig.4.4 and fig.4.5). To improve response of simplified models in which coarse background meshes are used (80cm and 120cm) zones near the pile tip are locally refined.

Material properties of the subsoil represented by a perfect elastic-plastic Mohr-Coulomb constitutive model are summarized in table 4.1 while properties of the pile are summarized in table 4.2.

Group	Parameter	Unit	Value
Elastic	$E$	[kPa]	60000
	$\nu$	[-]	0.3
Unit weight	$\gamma$	[kN/m <sup>3</sup> ]	20.0
Nonlinear	$\phi$	[°]	30
	$\psi$	[°]	0
	$c$	[kPa]	10

Table 4.1: Material properties of subsoil

Group	Parameter	Unit	Value
Elastic	$E$	[kPa]	300000000
	$\nu$	[-]	0.2
Unit weight	$\gamma$	[kN/m <sup>3</sup> ]	24/5

Table 4.2: Material properties of pile (in simplified models  $\gamma = 5 \text{ kN/m}^3$ )

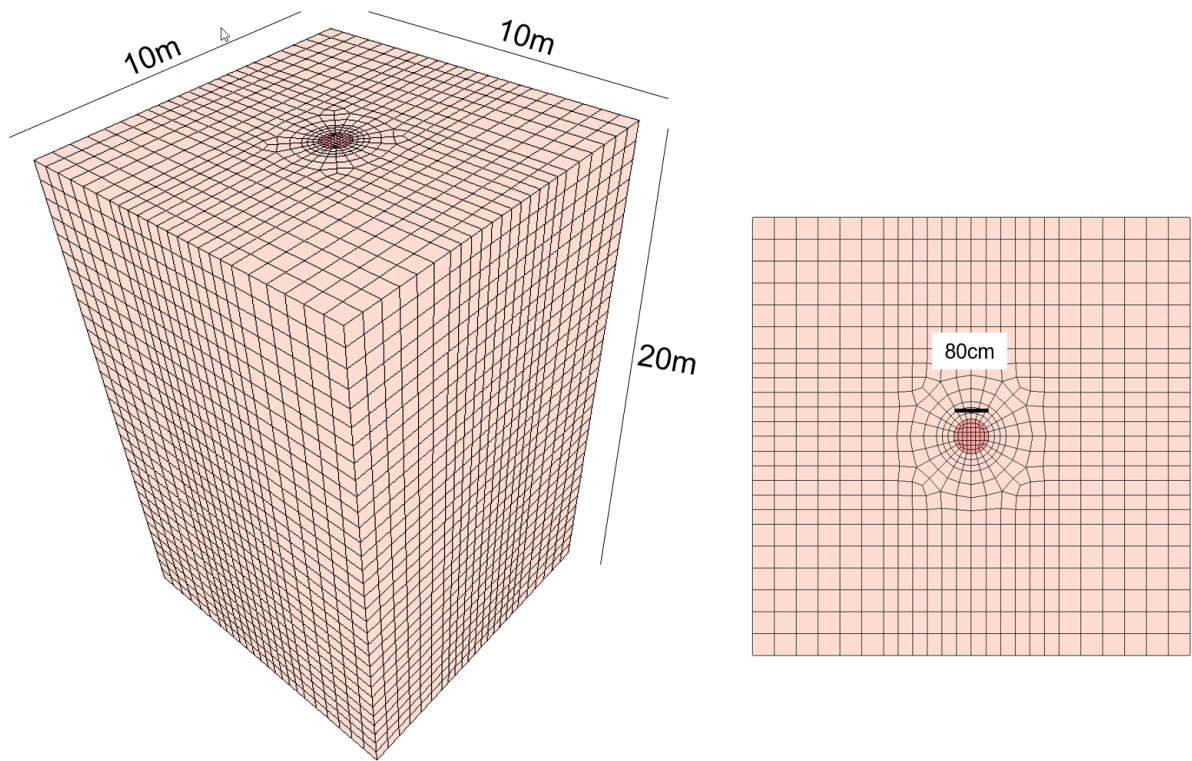


Figure 4.1: 3D reference model (subsoil and pile are discretized using 8 node brick continuum elements)

Comparison of the resulting pile axial force vs pile head settlement curves is shown in fig.4.7. It is well visible that for dense meshes a simplified model yields practically identical results



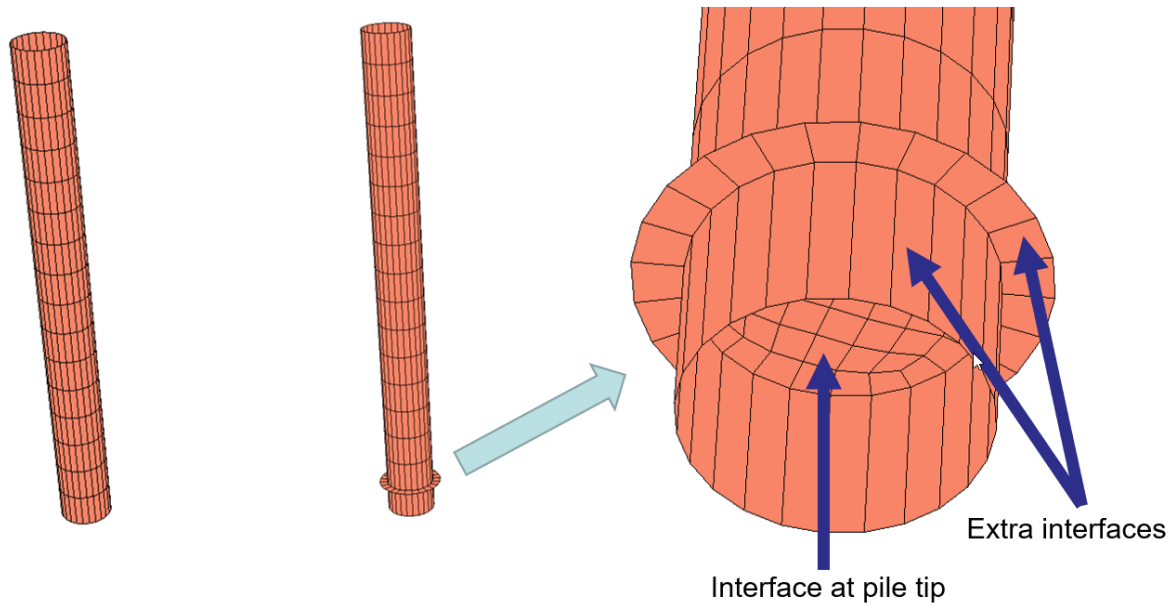


Figure 4.2: Contact interface setup for the reference 3D model (left plot) and enhanced model (right plot)

with the one obtained for the 3D reference model and a small deviation is observed for the grid size of 80cm. For grid of order of 120cm overshoot is larger. An important improvement is observed when the background mesh near the pile tip zone is locally refined (see fig.4.6). The major results mismatch is observed for coarse meshes once the shaft resistance is fully mobilized. It is worth mentioning that the vertical load density is amplified by the factor 1.011516313 as the circular pile cross section discretized using 3D elements is not equal to the exact circle area.

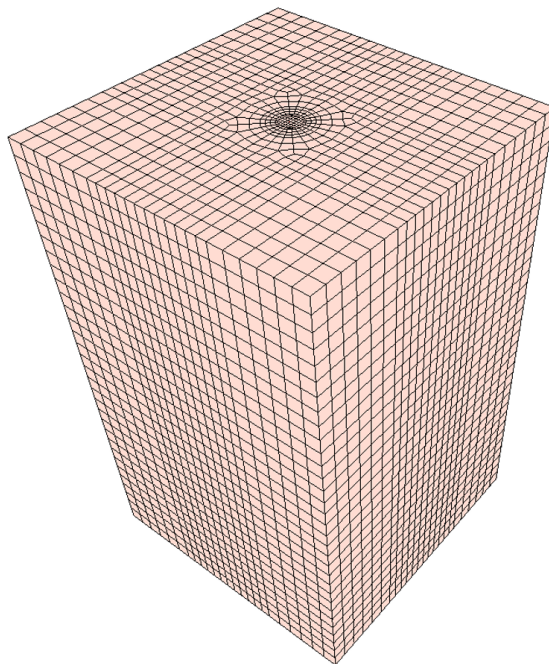


Figure 4.3: 3D model of a pile as a set of beam elements embedded in the 3D continuum (mesh compatible with the reference true 3D model)

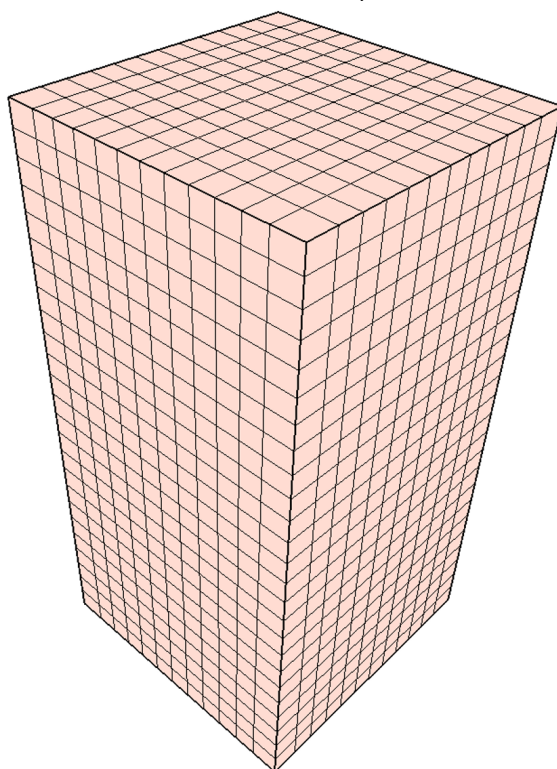


Figure 4.4: 3D model of a pile as a set of beam elements embedded in the 3D continuum (uniform grid with the horizontal element size  $h^e=80\text{cm}$ ) ( $h^e=64\text{cm}$  in the vertical direction)

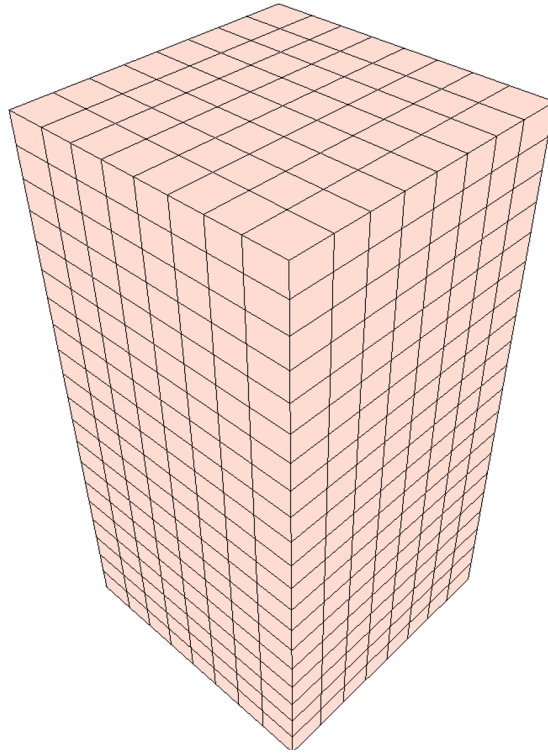


Figure 4.5: 3D model of a pile as a set of beam elements embedded in the 3D continuum (uniform grid with the horizontal element size  $h^e=120\text{cm}$ ) ( $h^e=80\text{cm}$  in the vertical direction)

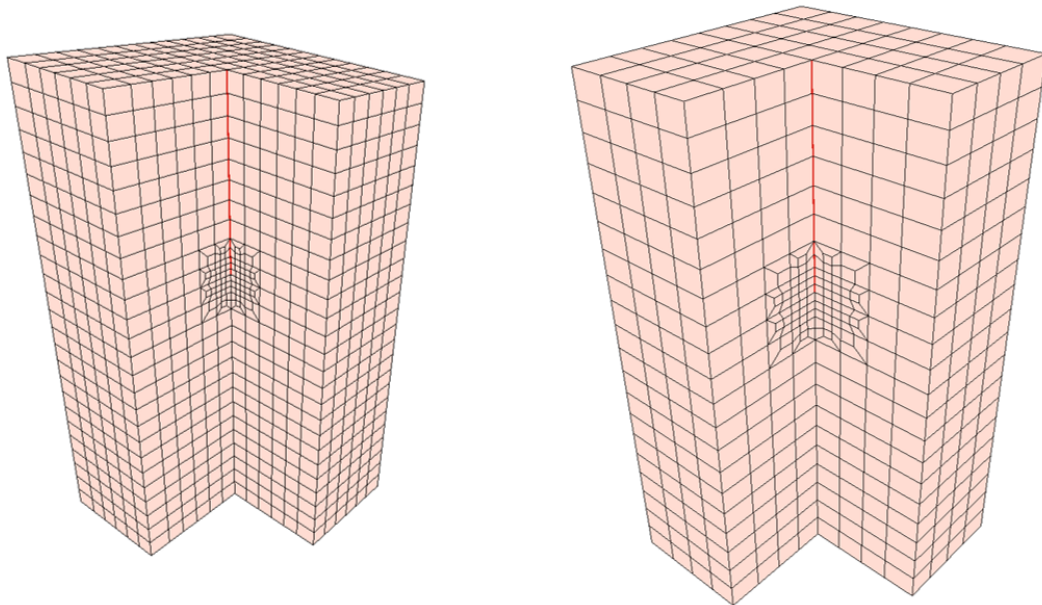


Figure 4.6: Mesh refinements near the pile tip for grids 80cm (left) and 120cm (right)

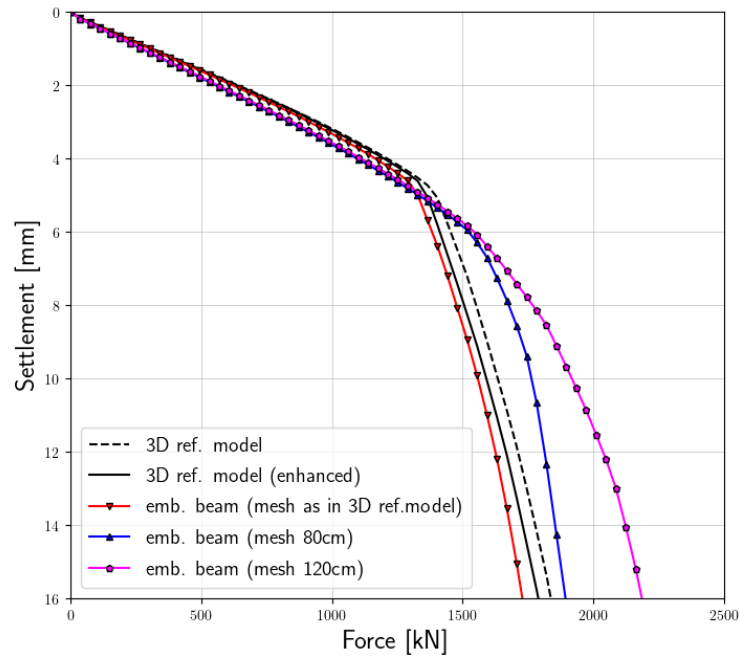


Figure 4.7: Axially loaded pile: comparizon of the resulting force-settlement curves (without tip zone refinement)

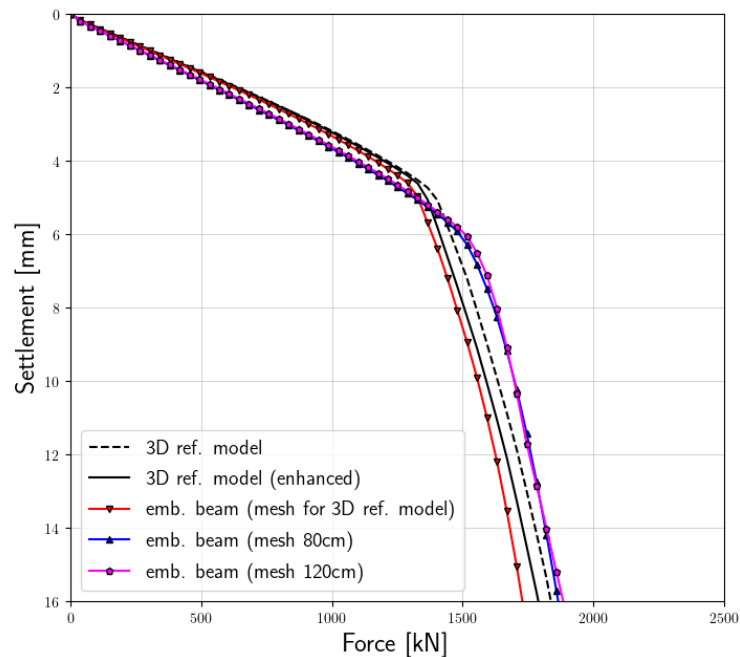


Figure 4.8: Axially loaded pile: comparizon of the resulting force-settlement curves (with local mesh refinement near the tip zone for grids 80cm and 120cm)

## 4.2 Circular pile subject to horizontal loading

Input files:

pile-horiz-3D-cont-frict.inp,  
 pile-horiz-embb-mesh-as-3D-frict.inp,  
 pile-horiz-embb-mesh-80cm-frict.inp,  
 pile-horiz-embb-mesh-120cm-frict.inp,  
 pile-horiz-embb-mesh-80cm-tip-refined-frict.inp,  
 pile-horiz-embb-mesh-120cm-tip-refined-frict.inp,

In this benchmark results of the full 3D model of an 8m long circular pile ( $\phi = 80\text{cm}$ ) subject to the horizontal loading (applied in global X-direction) are compared with the results obtained using the new embedding method of beam elements within the 3D continuum background mesh. The analyzed discretizations and material data are the same as in the benchmark for the axially loaded circular pile (see section 4.1).

Comparison of the force-horizontal displacement curves is shown in fig.4.10 and in fig.4.11 for meshes locally refined. It is well visible that local mesh refinement improves the results (refined meshes are shown in fig.4.9). In the following plots comparison of the pile deflection profiles and resulting bending moments is shown. In all cases simplified models yield slightly stiffer response than the true 3D reference model and local mesh refinement along whole pile axis improves quality of the results. In order to trace bending moment and deflection of the pile in the 3D reference model artificial beam elements are plugged in the 3D mesh with the scaled (by factor  $10^{-6}$ ) stiffness modulus (original pile cross section is used in the data set). For the high quality of the bending moment recovery using artificial beams horizontal loading is applied in the distributed form rather than the concentrated force. It is worth mentioning that this horizontal load density is amplified by the factor 1.011516313 as the circular pile cross section discretized using 3D elements is not equal to the exact circle area. Presented results show that the method is convergent and no pathological mesh dependency is observed in the new embedding method.

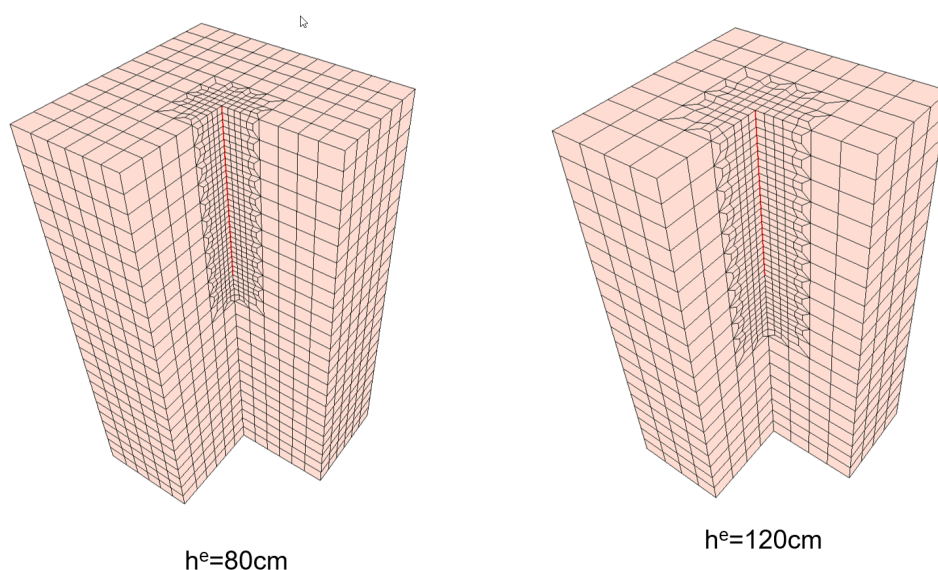


Figure 4.9: Local mesh refinements along whole pile axis

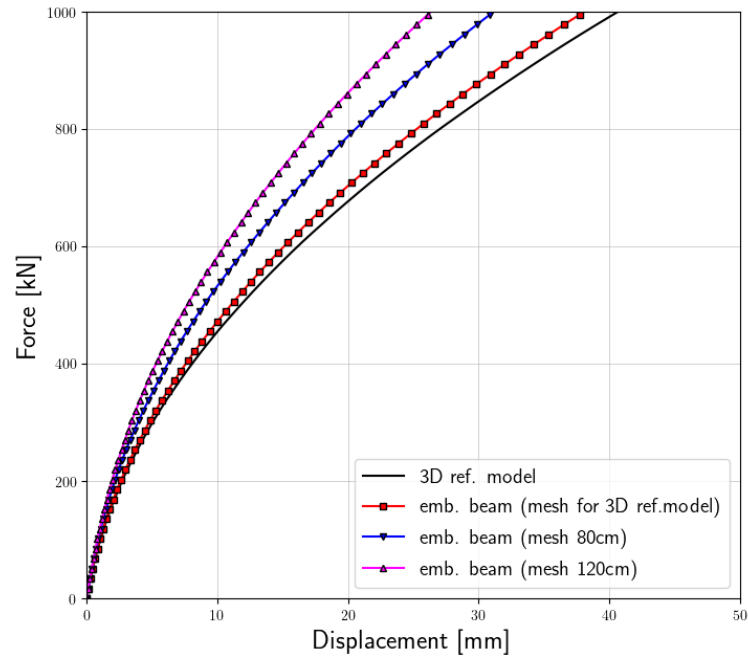


Figure 4.10: Comparizon of force-displacement diagrams for horizontally loaded pile

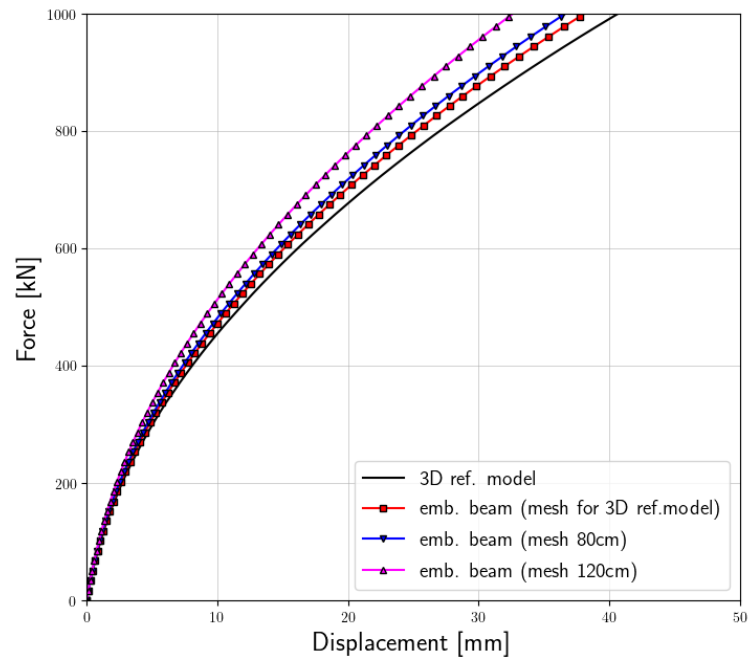


Figure 4.11: Comparizon of force-displacement diagrams for horizontally loaded pile for locally refined meshes

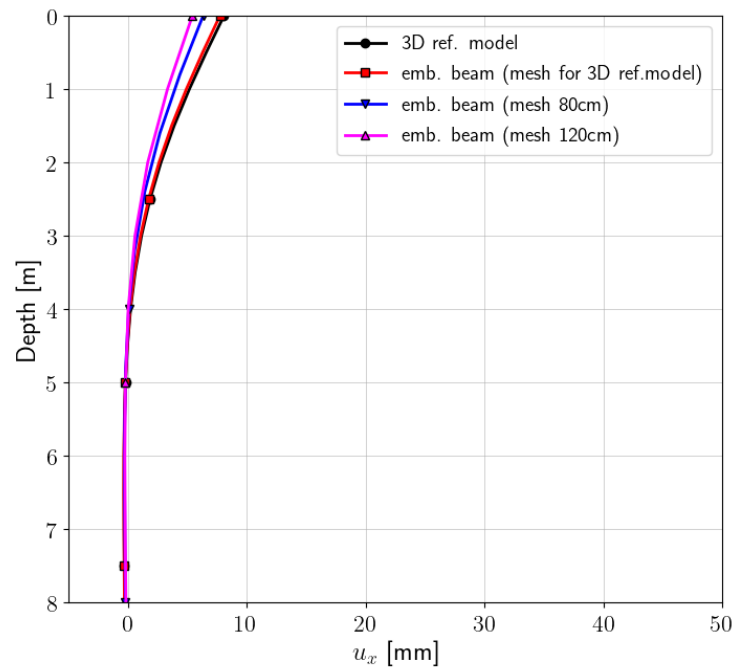


Figure 4.12: Profile of pile deflection under force  $H = 400$  kN

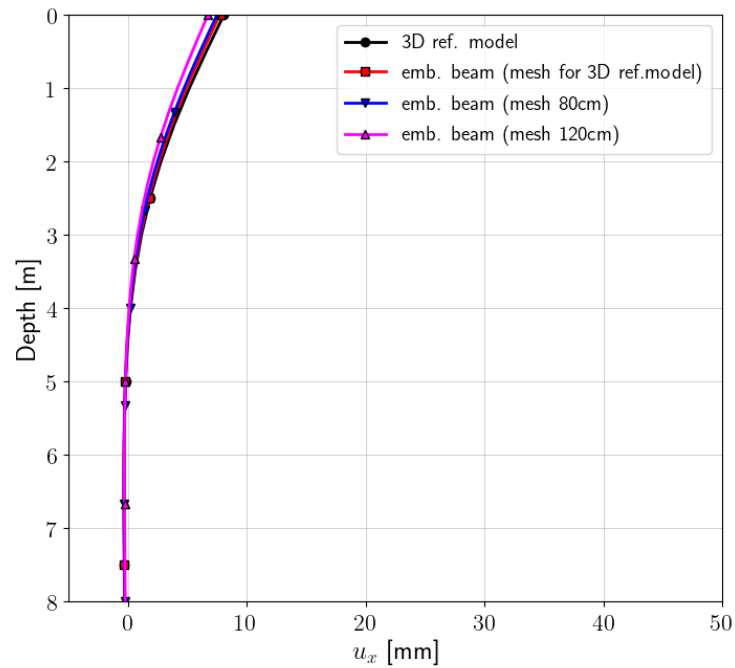


Figure 4.13: Profile of pile deflection under force  $H = 400$  kN for locally refined meshes

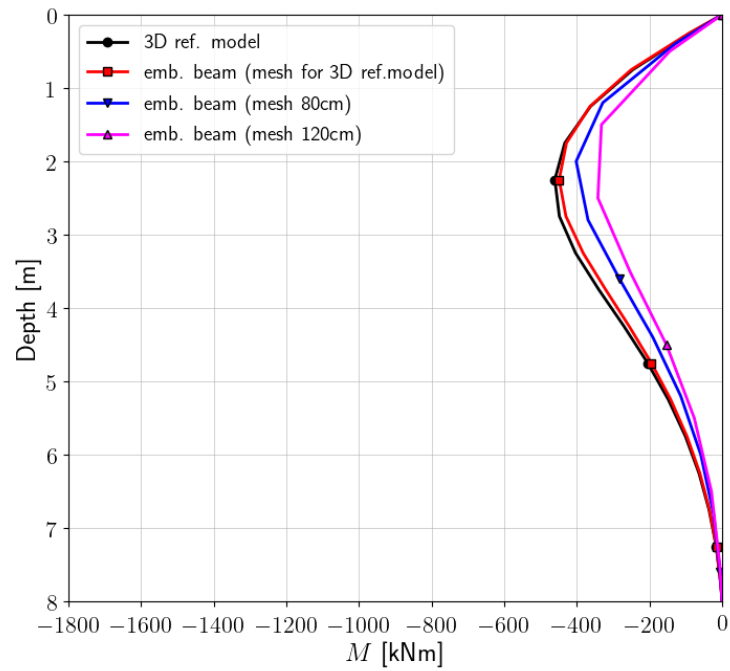


Figure 4.14: Profile of the bending moment under force  $H = 400$  kN

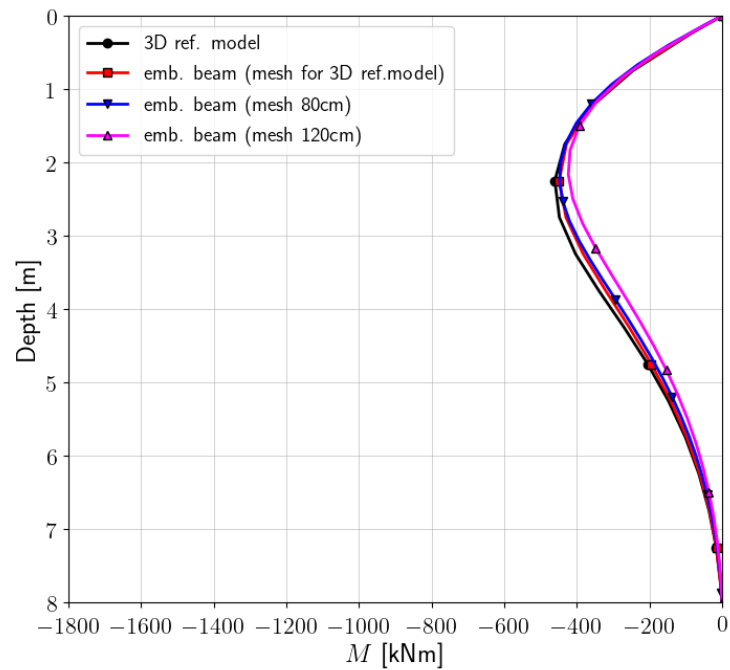


Figure 4.15: Profile of the bending moment under force  $H = 400$  kN for locally refined meshes



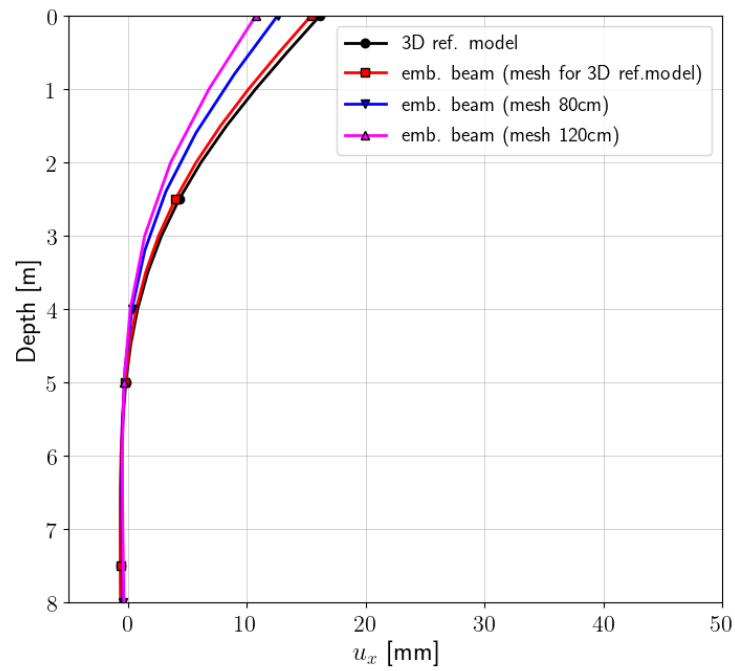


Figure 4.16: Profile of pile deflection under force  $H = 600$  kN

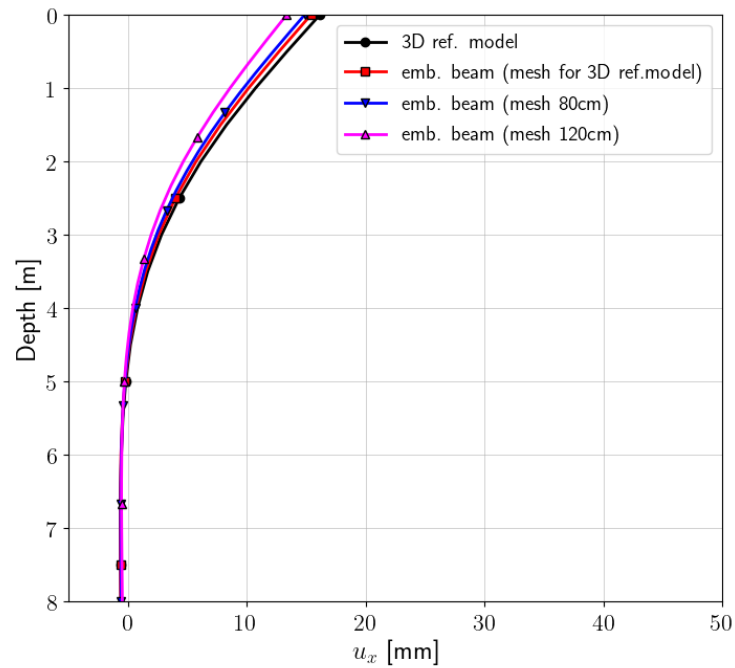


Figure 4.17: Profile of pile deflection under force  $H = 600$  kN for locally refined meshes

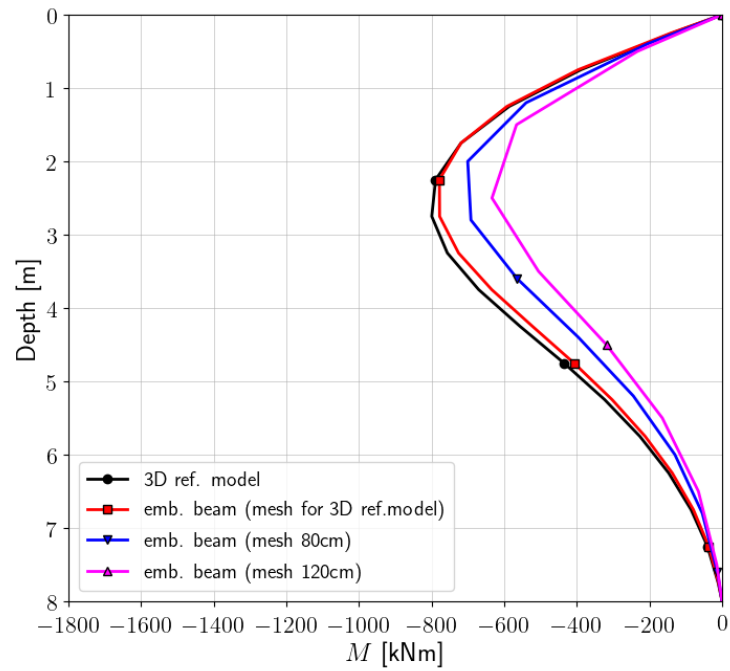


Figure 4.18: Profile of the bending moment under force  $H = 600$  kN

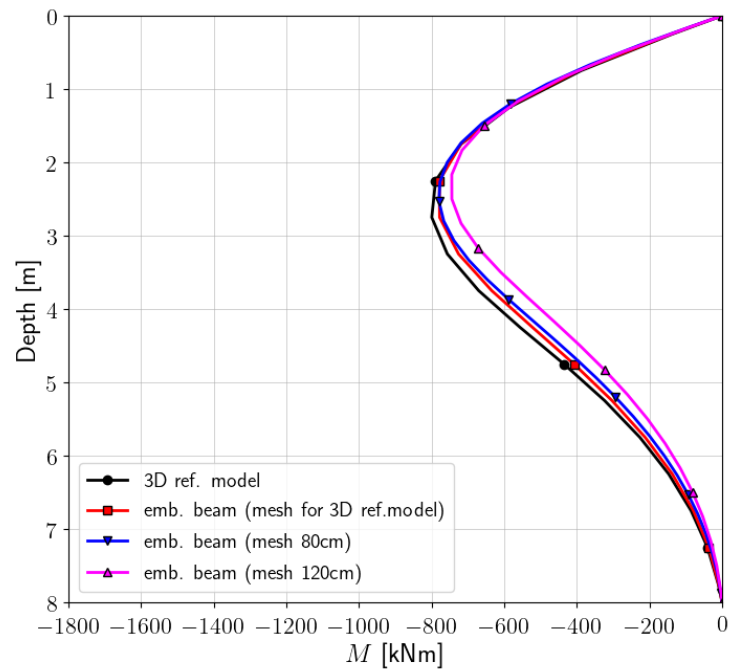


Figure 4.19: Profile of the bending moment under force  $H = 600$  kN for locally refined meshes

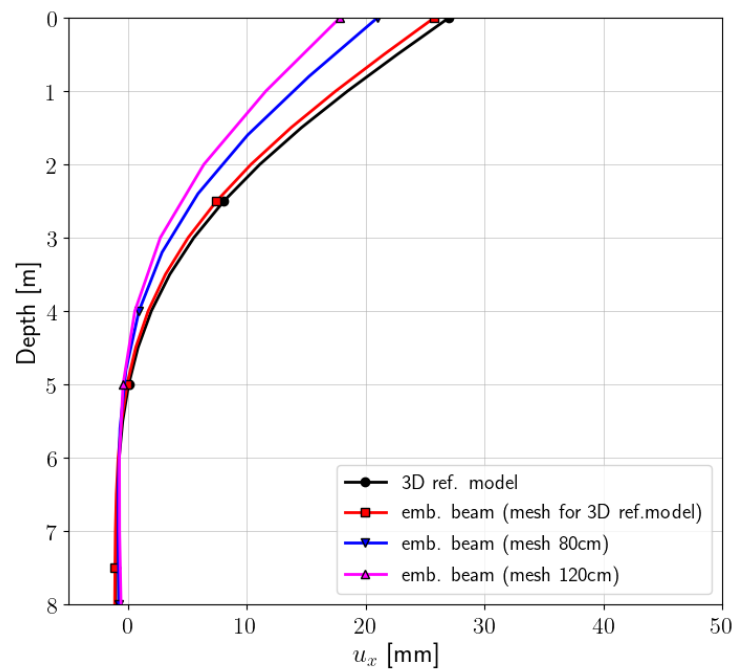


Figure 4.20: Profile of pile deflection under force  $H = 800$  kN

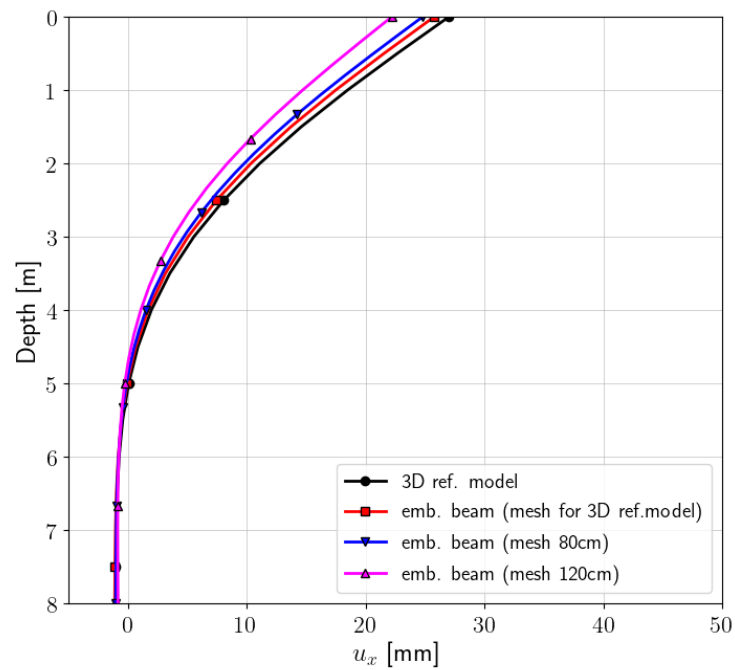


Figure 4.21: Profile of pile deflection under force  $H = 800$  kN for locally refined meshes

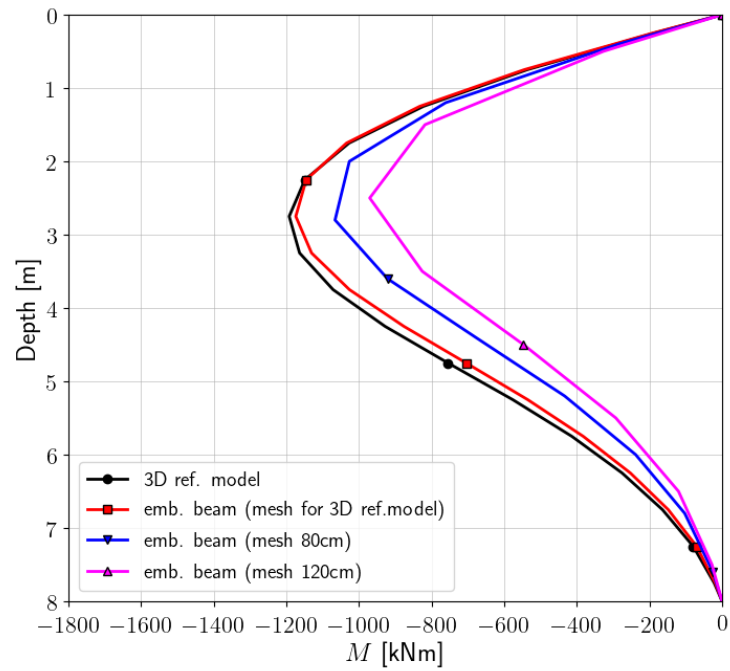


Figure 4.22: Profile of the bending moment under force  $H = 800$  kN

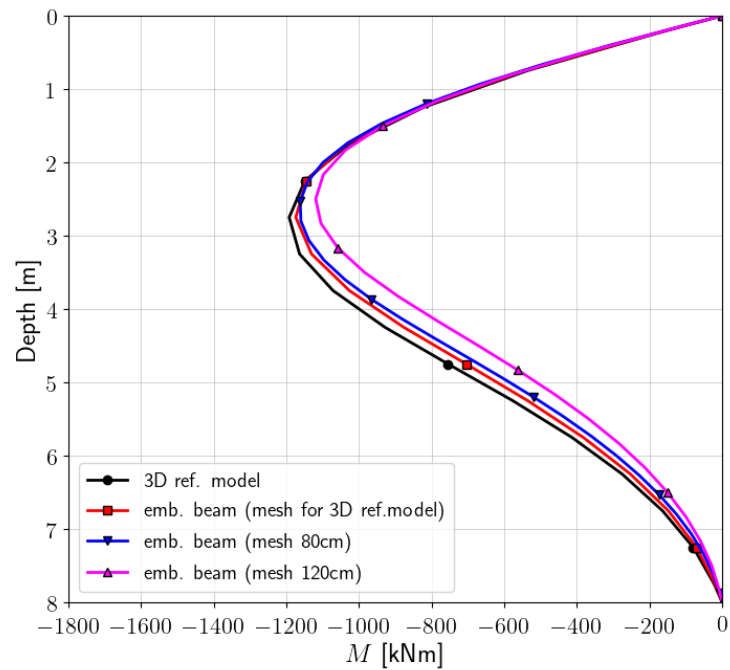


Figure 4.23: Profile of the bending moment under force  $H = 800$  kN for locally refined meshes

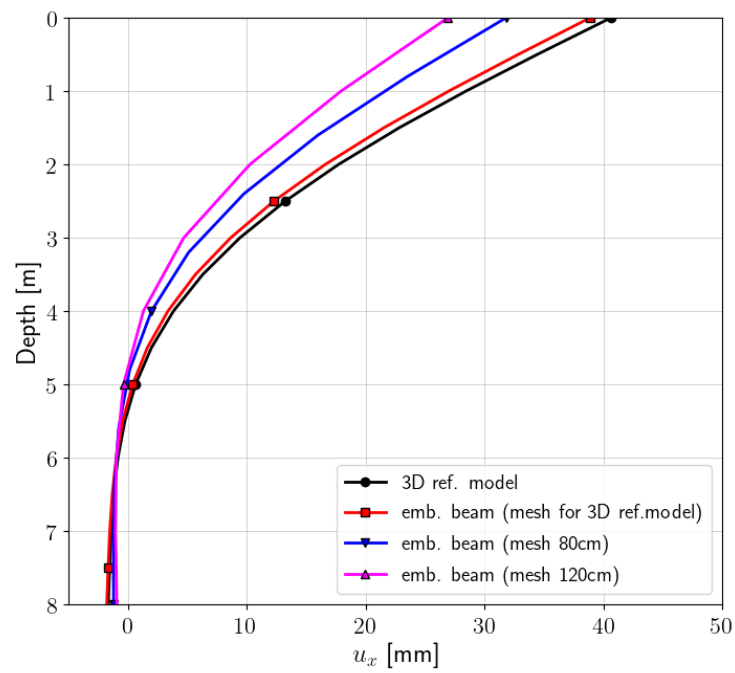


Figure 4.24: Profile of pile deflection under force  $H = 1000$  kN

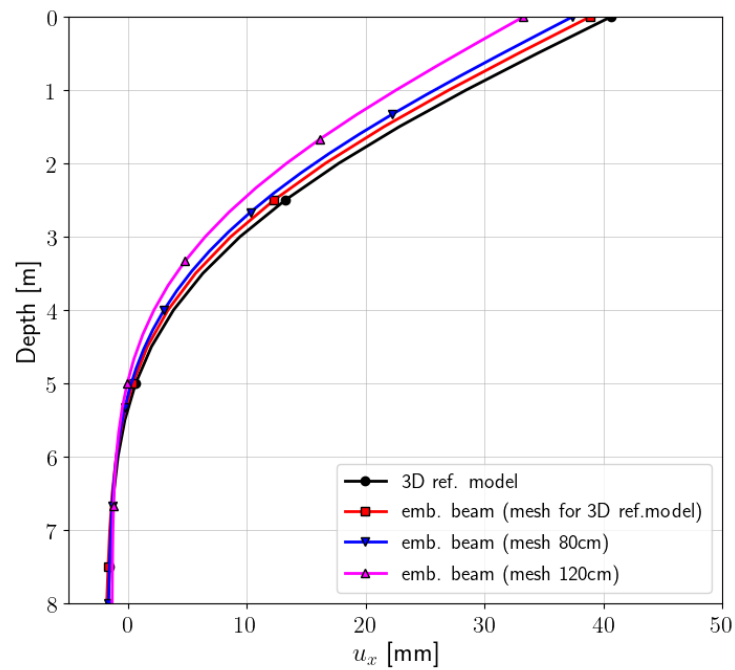


Figure 4.25: Profile of pile deflection under force  $H = 1000$  kN for locally refined meshes

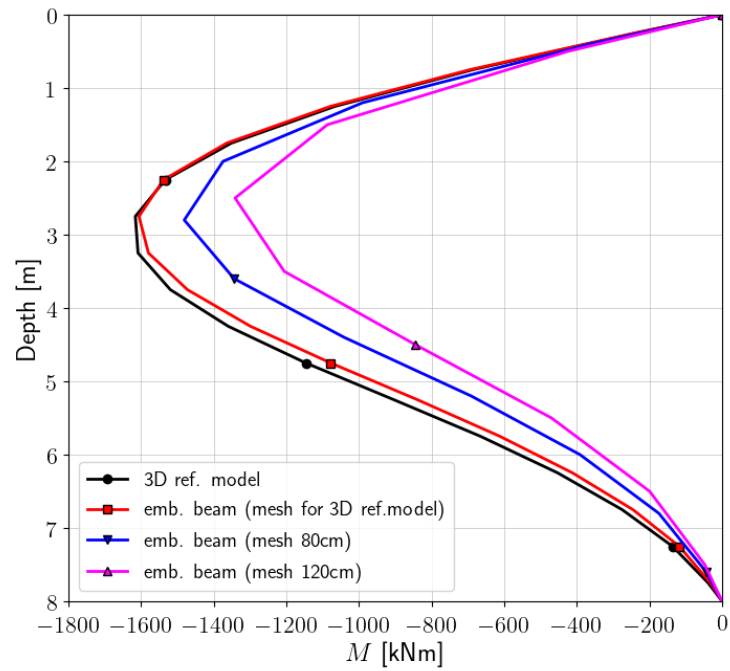


Figure 4.26: Profile of the bending moment under force  $H = 1000$  kN

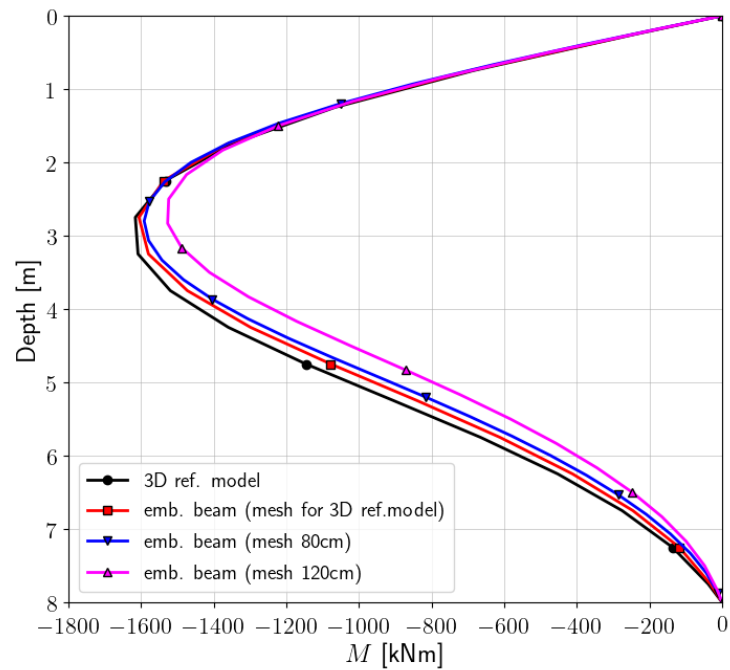


Figure 4.27: Profile of the bending moment under force  $H = 1000$  kN for locally refined meshes

### 4.3 Barette subject to axial loading

Input files:

barette-axial-3D-cont-frict.inp,  
 barette-axial-3D-cont-frict-with-tip-cnt-ex.inp,  
 barette-axial-embb-mesh-as-3D-frict.inp,  
 barette-axial-embb-mesh-40cm-frict.inp,  
 barette-axial-embb-mesh-80cm-frict.inp,  
 barette-axial-embb-mesh-40cm-tip-refined-frict.inp,  
 barette-axial-embb-mesh-80cm-tip-refined-frict.inp

In this section an axial load test carried out on the 8m long barette (cross section 160x80cm) is analyzed. The reference 3D model is discretized using 8 node brick elements. Subsoil is modeled using perfect elasto-plastic Mohr-Coulomb model. Material properties used in this benchmark are summarized in tables 4.3 and 4.4.

Results of the reference model are then compared with the results of simplified models in which the barette is treated as a set of beam elements embedded in the 3D continuum using non-local embedding method.

The 3D mesh of the reference model is shown in the fig.4.28. Two contact interface setups are considered, the one with the skin interface only and the second one with additional interface at the barette tip but also extra interfaces in the zone of the shaft-barette tip surfaces intersection (see fig.4.29).

The simplified method is verified using three different meshes. In the first simplified model the background mesh is equivalent to the mesh of the full 3D reference model (see fig.4.30). In the next two simplified models with the uniform grid size (in X-Z plane) 40cm and 80cm are used (see fig.4.31 and fig.4.32). To improve response of simplified models in which coarse background meshes are used (40cm and 80cm) zones near the barette tip are locally refined.

Material properties of the subsoil represented by a perfect elastic-plastic Mohr-Coulomb constitutive model are summarized in table 4.3 while properties of the barette are summarized in table 4.4.

Group	Parameter	Unit	Value
Elastic	$E$	[kPa]	60000
	$\nu$	[-]	0.3
Unit weight	$\gamma$	[kN/m <sup>3</sup> ]	20.0
Nonlinear	$\phi$	[°]	30
	$\psi$	[°]	0
	$c$	[kPa]	10

Table 4.3: Material properties of subsoil

Group	Parameter	Unit	Value
-------	-----------	------	-------

Elastic	$E$	[kPa]	30000000
	$\nu$	[-]	0.2
Unit weight	$\gamma$	[kN/m <sup>3</sup> ]	24/5

Table 4.4: Material properties of barette (in simplified models  $\gamma = 5 \text{ kN/m}^3$ )

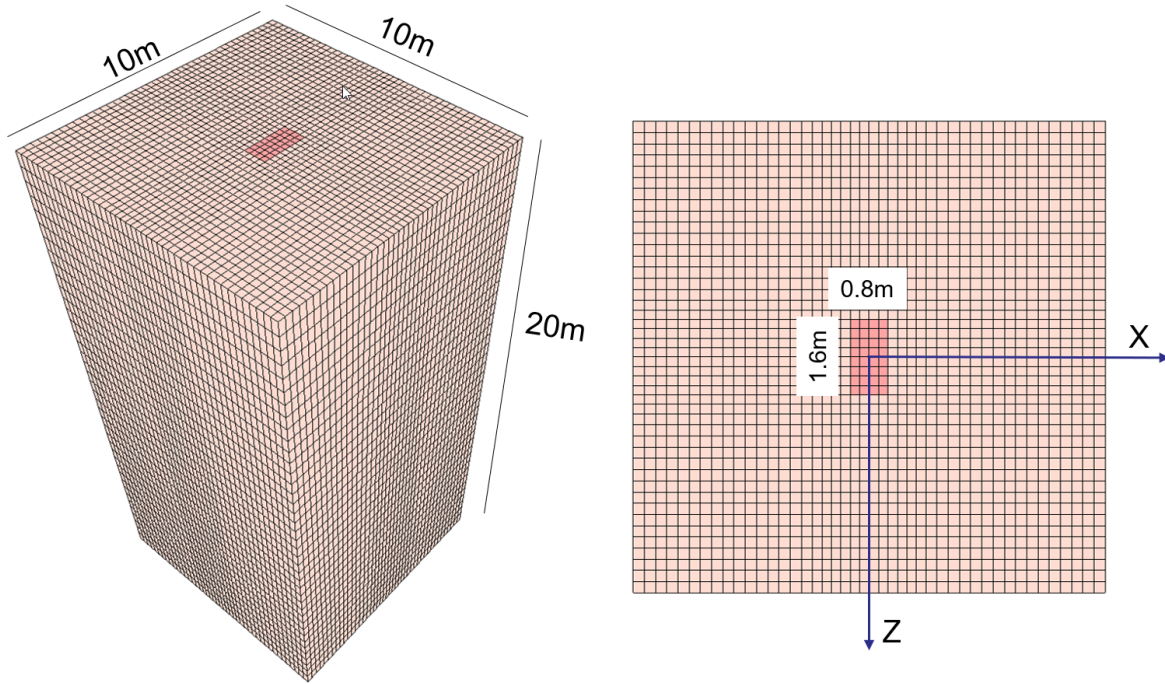


Figure 4.28: 3D reference model (subsoil and barette are discretized using 8 node brick continuum elements)

Comparison of the resulting barette axial force vs barette head settlement curves is shown in fig.4.34. It is well visible that results for simplified models based on coarser meshes are quite close to the results of the two true 3D reference models. Result for the simplified model based on the same mesh as the reference 3D model yields slightly softer response. Again an important improvement is observed when the tip zone is locally refined.



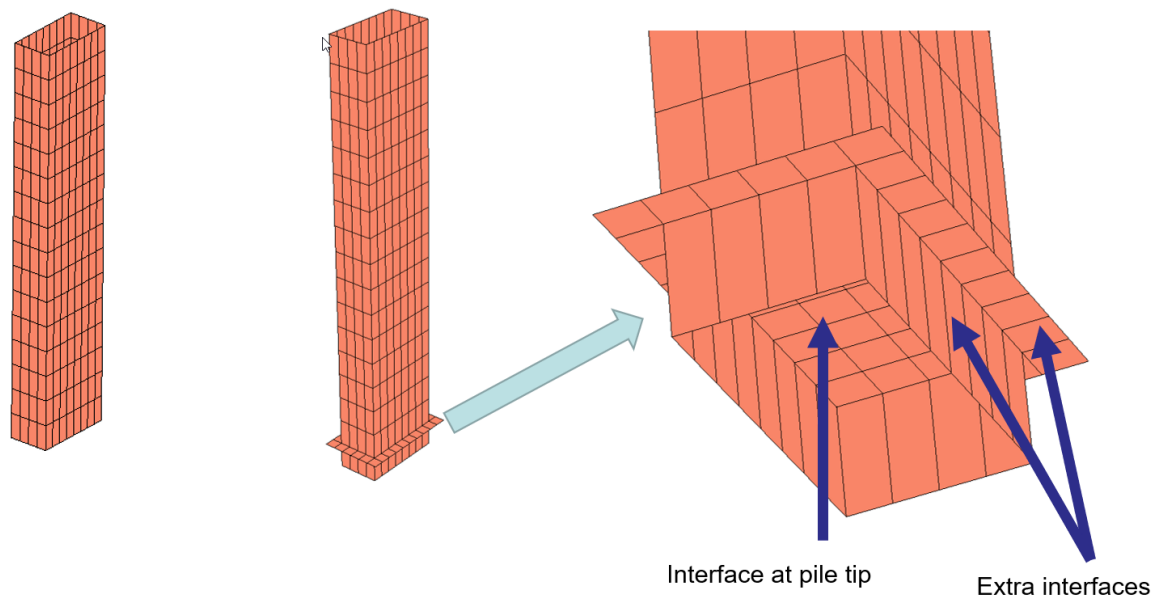


Figure 4.29: 3D reference model (subsoil and barette are discretized using 8 node brick continuum elements)

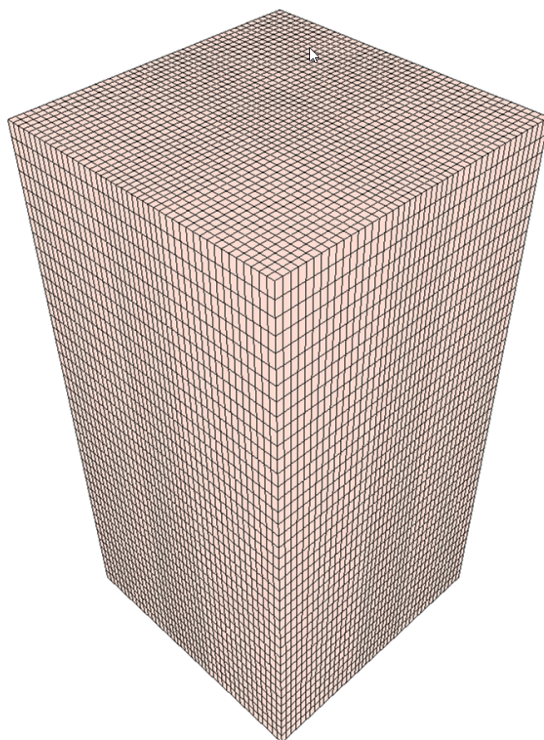


Figure 4.30: 3D model of a barette as a set of beam elements embedded in the 3D continuum (mesh compatible with the reference true 3D model)

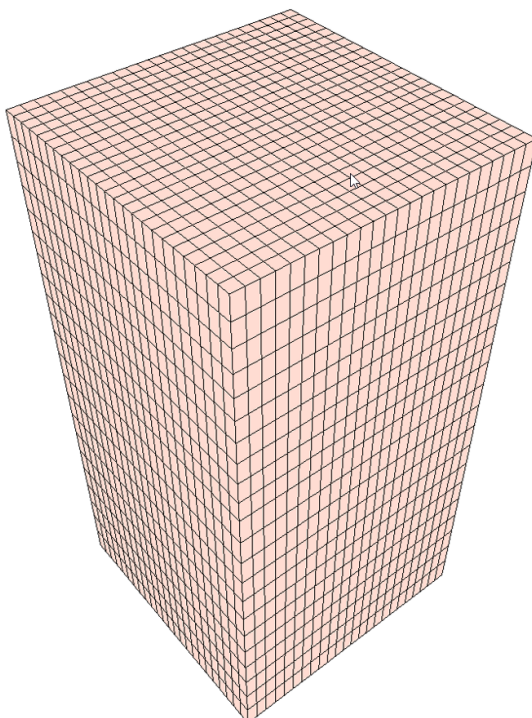


Figure 4.31: 3D model of a barette as a set of beam elements embedded in the 3D continuum (uniform grid in X-Z plane  $h^e=40\text{cm}$ ) ( $h^e=80\text{cm}$  in the vertical direction)

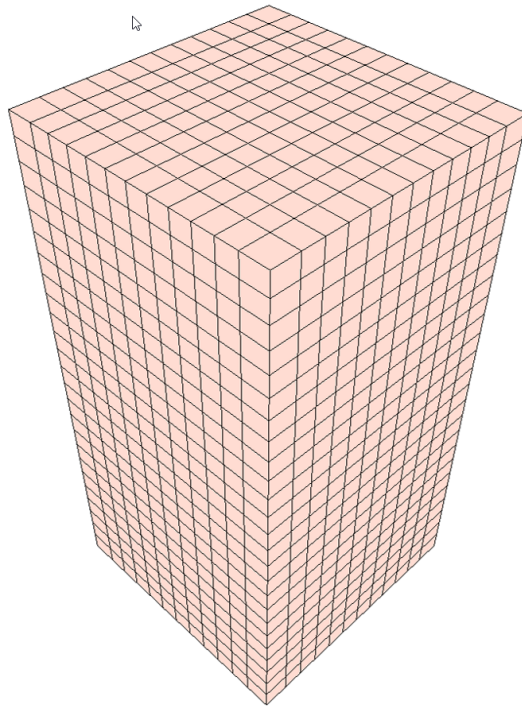


Figure 4.32: 3D model of a barette as a set of beam elements embedded in the 3D continuum (uniform grid in X-Z plane  $h^e=80\text{cm}$ ) ( $h^e=80\text{cm}$  in the vertical direction)

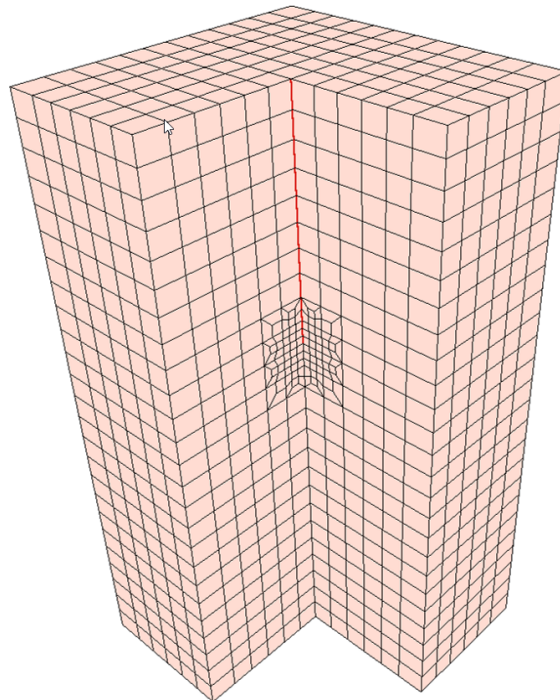


Figure 4.33: Mesh refinement near the barette tip for grid size 80cm

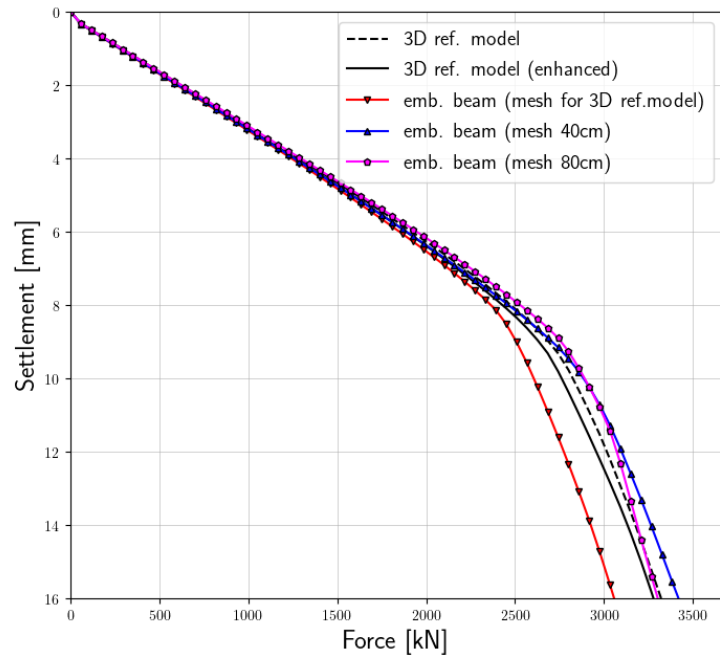


Figure 4.34: Axially loaded barett: comparizon of the resulting force-settlement curves (without tip zone refinement)

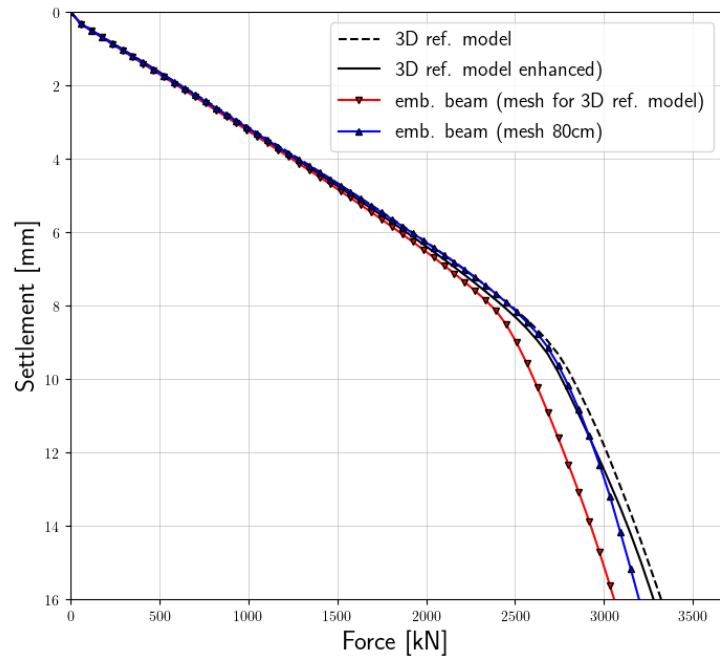


Figure 4.35: Axially loaded barett: comparizon of the resulting force-settlement curves (with local mesh refinement near the tip zone for grids 80cm and 120cm)

## 4.4 Barette subject to horizontal loading

Input files:

barette-horiz-3D-cont-frict.inp,  
 barette-horiz-emb-mesh-as-3D-frict.inp,  
 pile-horiz-emb-mesh-40cm-frict.inp,  
 pile-horiz-emb-mesh-80cm-frict.inp

In this benchmark results of the full 3D model of an 8m long barette (cross section 160x80cm) subject to the horizontal loading (applied in global X-direction) are compared with the results obtained using the new embedding method of beam elements within the 3D continuum background mesh. The analyzed discretizations and material data are the same as in the benchmark for the axially loaded barette (see section 4.3).

Comparison of the force-horizontal displacement curves is shown in fig.4.36. In the following plots comparison of the barette deflection and resulting bending moments profiles are shown. In all cases simplified models yield slightly stiffer response than the true 3D reference model. In order to trace bending moment and deflection of the barette in the 3D reference model artificial beam elements are plugged in the 3D mesh with the scaled (by factor  $10^{-6}$ ) stiffness modulus (original barette cross section is used in the data set). For the high quality of the bending moment recovery using artificial beams horizontal loading is applied as a distributed rather than the concentrated force. Presented results show that the method is convergent and no pathological mesh dependency is observed in the new embedding method.

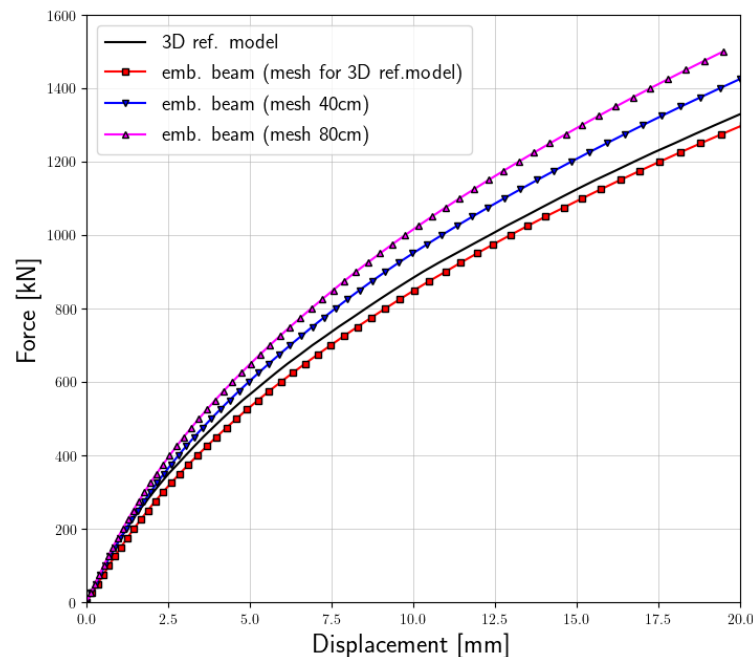


Figure 4.36: Comparison of force-displacement diagrams for horizontally loaded barette

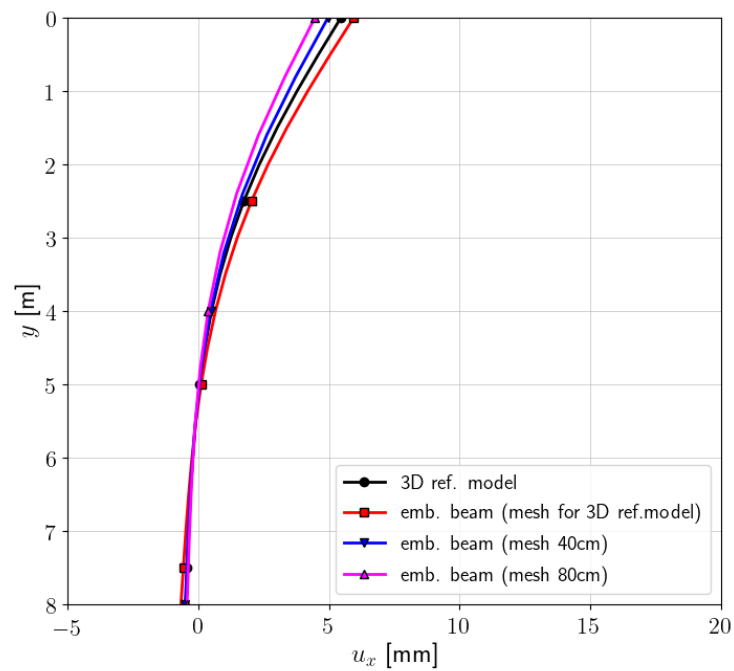


Figure 4.37: Profile of barett deflection under force  $H = 600$  kN

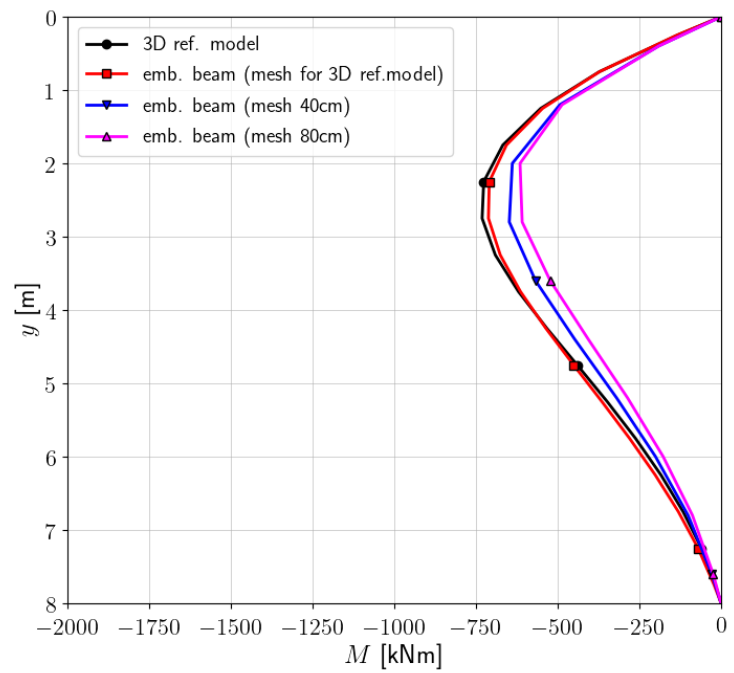


Figure 4.38: Profile of the bending moment under force  $H = 600$  kN

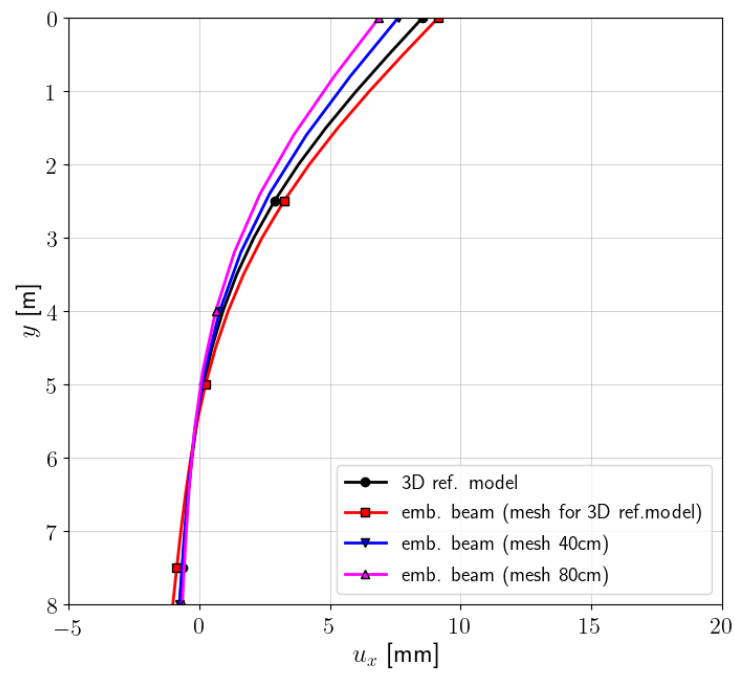


Figure 4.39: Profile of barette deflection under force  $H = 800$  kN

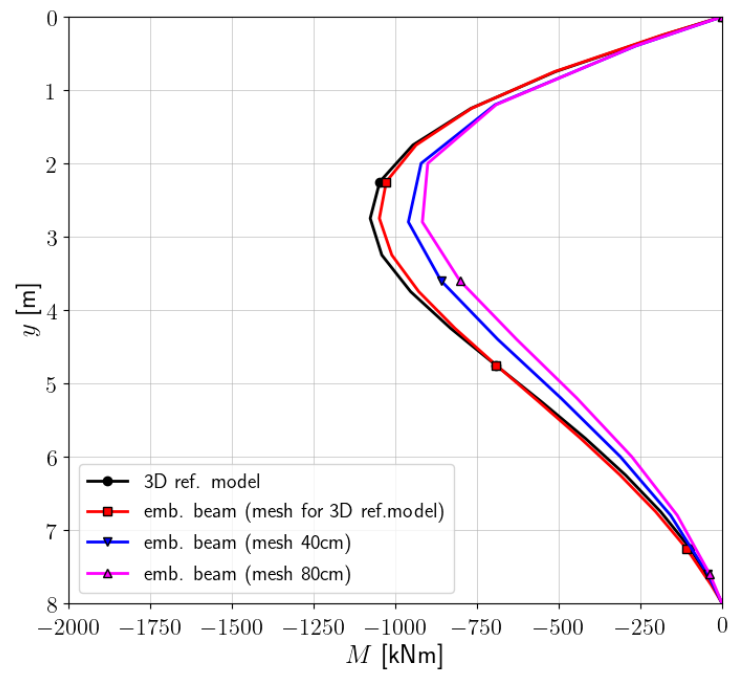


Figure 4.40: Profile of the bending moment under force  $H = 800$  kN

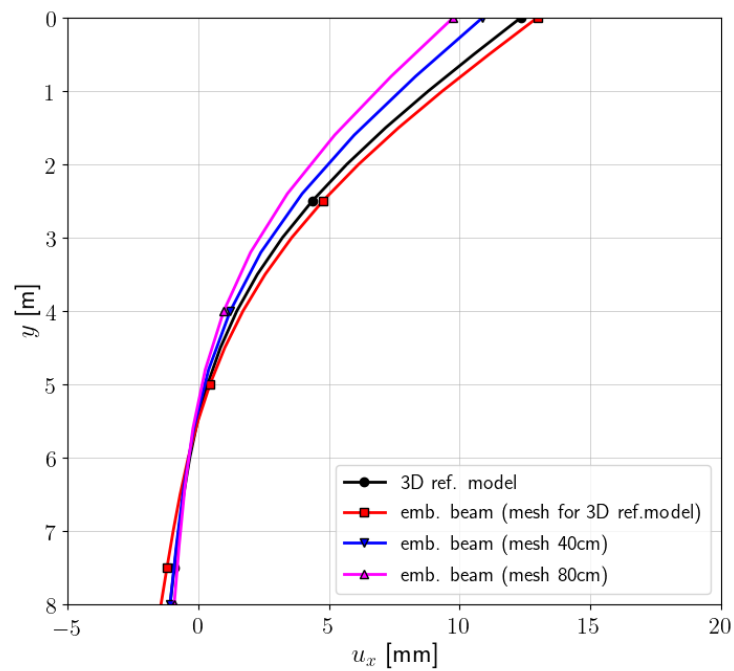


Figure 4.41: Profile of baretté deflection under force  $H = 1000$  kN

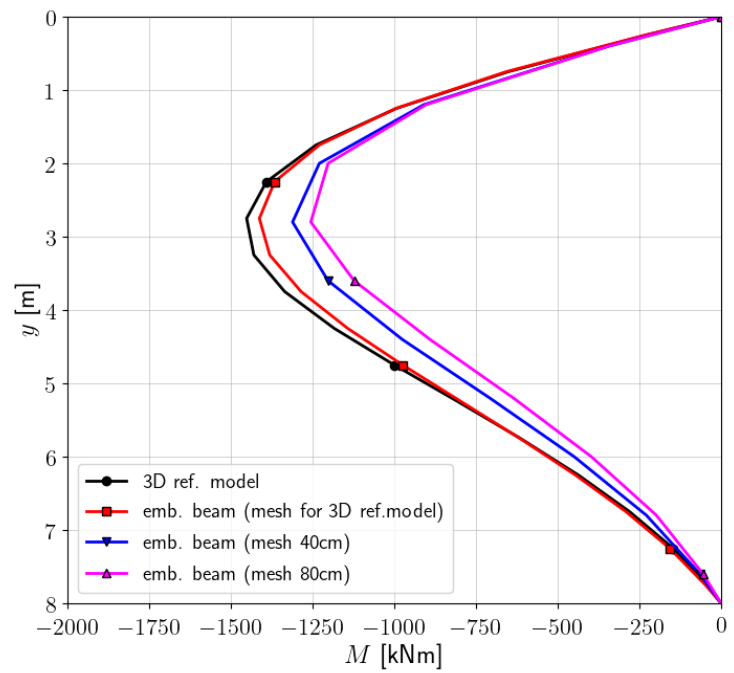


Figure 4.42: Profile of the bending moment under force  $H = 1000$  kN



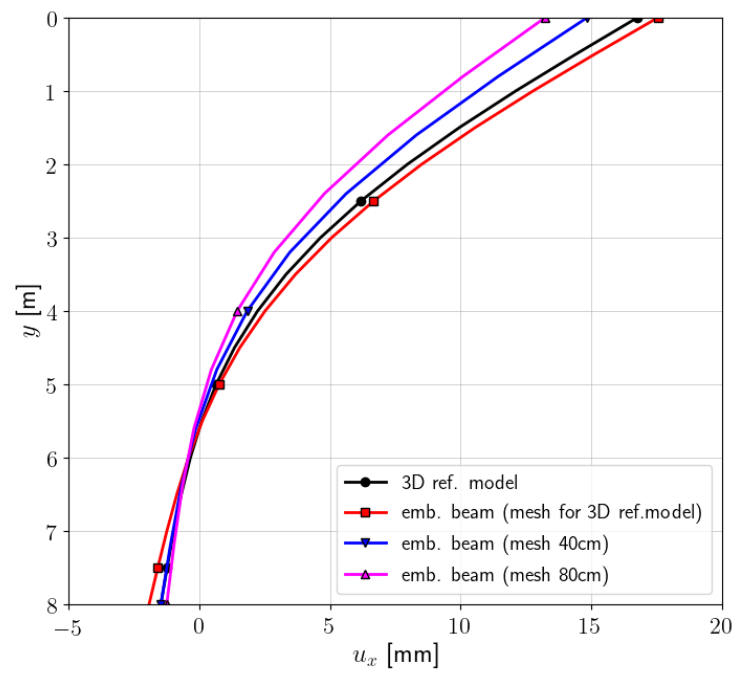


Figure 4.43: Profile of barette deflection under force  $H = 1200$  kN

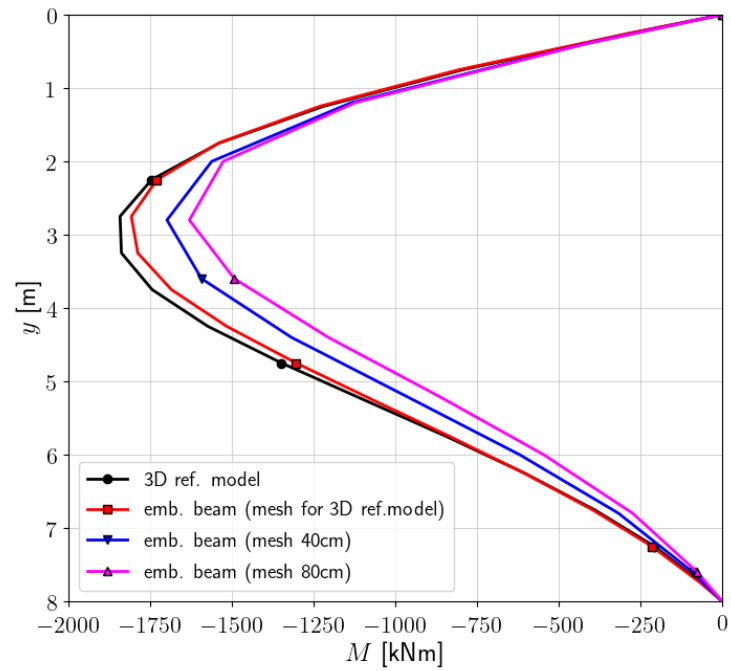


Figure 4.44: Profile of the bending moment under force  $H = 1200$  kN

## 4.5 Foundation raft

### Input files:

raft-cont-3D.inp,  
 raft-emb-mesh-grid-40x40cm-piles-off.inp,  
 raft-emb-mesh-grid-40x40cm-piles-60cm.inp,  
 raft-emb-mesh-grid-40x40cm-piles-60cm-dense-tip.inp,  
 raft-emb-mesh-grid-80x80cm-piles-off.inp,  
 raft-emb-mesh-grid-80x80cm-piles-60cm.inp,  
 raft-emb-mesh-grid-80x80cm-piles-60cm-dense-tip.inp

In this section a rectangular, 1.5m thick, RC foundation raft (40m x 32m), installed 3m below ground level and subject to a uniform loading 300 kN/m<sup>2</sup> is analyzed. In order to diminish total and relative settlements of the raft it is strengthened by 12m long circular piles (diameter  $\phi = 60$  cm). In the course of the carried out analyses settlements of the raft without piles were computed first and then the new embedding method was verified, using different discretizations and local mesh refinements in the vicinity of pile tips. To cancel the effect of overshooting the normal force transferred through the pile tip a normal stress cut-off condition is activated (the maximum normal stress under pile tip in third soil layer is limited here by the value 2000 kPa). The general 3D setup of the analyzed problem (for mesh with the X-Z plane grid size 80cm), including 2 symmetry planes X-Y and Z-Y, is shown in fig.4.45. Piles location (4m spacing in both directions) is shown in the fig.4.46. To reduce size of the computational model the excavation procedure is run in a simplified manner by superposing two sets of surface loadings, as shown in the fig.4.47. Subsoil consists of three soil layers ie. sands up to depth of 3m, soft cohesive soil till the depth of 6m and then sandy silts. These layers are modeled using the HS-Brick model. The assumed set of model parameters is given in table 4.5. Piles and foundation raft are represented by an linear-elastic model with parameters summarized in table 4.6. Strength and dilatancy parameters of the pile-subsoil interface zone are handled in a relative manner with respect to the strength and dilatancy of subsoil layers. The following rule (index  $i$  refers to the interface) was applied in this benchmark (dilatancy is meaningful only in the case of the true 3D interface between piles modeled as a 3D continuum and subsoil).

$$\begin{aligned}\tan \phi_i &= k \tan \phi_{soil} \\ c_i &= k c_{soil} \\ \tan \psi_i &= k \tan \psi_{soil} \\ k &= 1\end{aligned}$$

In the considered case study the applied loading is sufficiently large to reach the ultimate skin friction and end pile bearing capacity. Therefore settlements at 2 levels of loading  $q = 150/300$  kN/m<sup>2</sup> are examined. Color contours of incremental settlements (reference time is assumed at the time of raft construction) for the case of the slab only (piles are not activated) for two mesh densities and two loading levels (150/300 kN/m<sup>2</sup>) are shown in fig.4.48, 4.49, 4.50, 4.51. In the next set of figures color contours of incremental settlements for the two meshes including local mesh refinements near pile tips are shown in fig. 4.52, 4.53, 4.54, 4.55, 4.56, 4.57, 4.58, 4.59. Summary of computed settlements is given in table4.7. All results are rounded to 1mm.

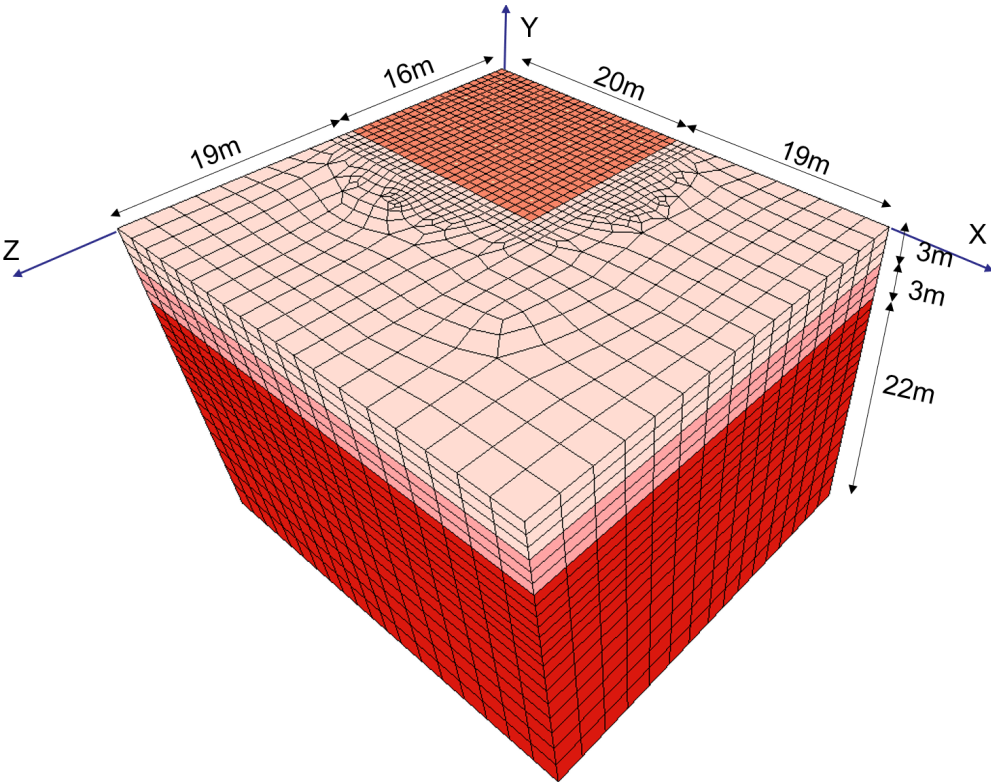


Figure 4.45: Foundation raft setup with 2 symmetry planes

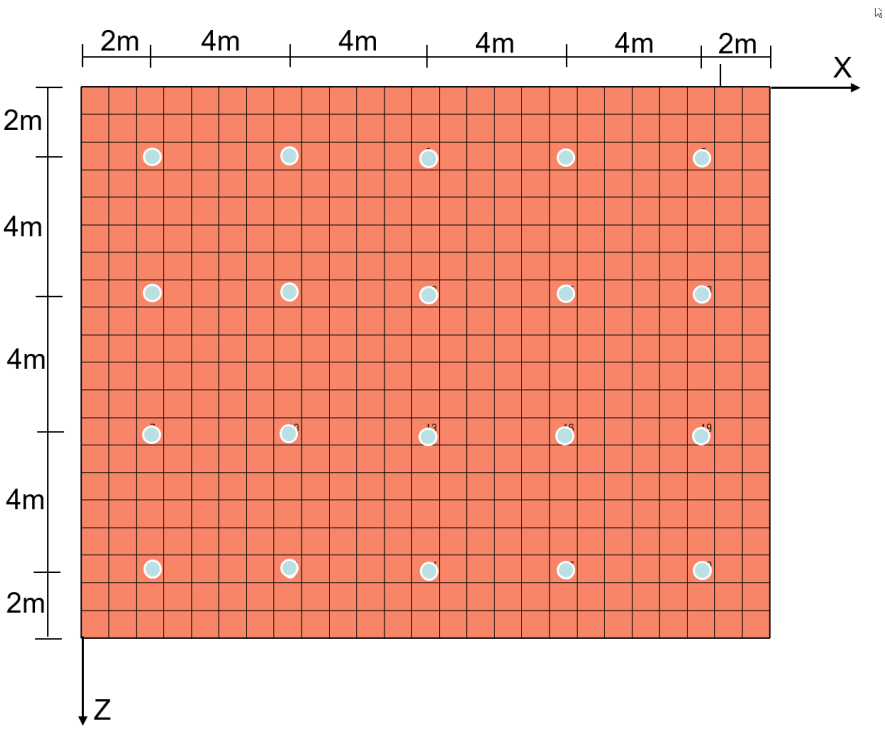


Figure 4.46: Piles location

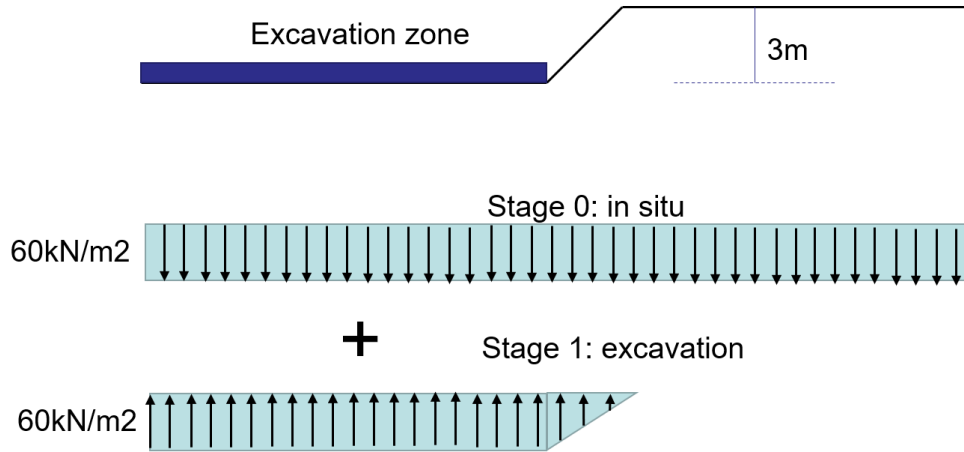


Figure 4.47: Simplified treatment of an excavation procedure. In the initial state (stage 0) the 3m of the overburden is replaced by surface loading 60 kN/m<sup>2</sup> applied to the whole top model surface, then in the stage of an excavation (stage 1) and inverse equivalent surface loading is added but only in the excavation zone.

Table 4.5: Material properties of soils

	Material	Model	Data group	Parameter	Unit	Value
1	Sands	HS-Brick	Elastic	$E_{ur}^{ref}$	[kN/m <sup>2</sup> ]	120000
				$\sigma_{ref}$	[kN/m <sup>2</sup> ]	100.0
				$\nu$	–	0.2
				$m$	–	0.50
				$\sigma_L$	[kN/m <sup>2</sup> ]	10.0
				barotropy	–	$p$
				$E_0^{ref}$	[kN/m <sup>2</sup> ]	360000
				$\gamma_{0.7}$	–	0.0002
			Unit weights	$\gamma$	[kN/m <sup>3</sup> ]	20
			Non-linear	$\phi$	[°]	36
				$\psi$	[°]	4
				$c$	[kN/m <sup>2</sup> ]	1
				$E_{50}^{ref}$	[kN/m <sup>2</sup> ]	40000
				$R_f$	–	0.9
				$D$	–	0.25
			Stress history	$OCR$	–	1.05
				$K_0^{NC}$	–	0.41
				$p_{c0}^{min}$	[kN/m <sup>2</sup> ]	10.0
2	soft soil	HS-Brick	Initial $K_0$ state	$K_0$	–	0.50
			Elastic	$E_{ur}^{ref}$	[kN/m <sup>2</sup> ]	36000
				$\sigma_{ref}$	[kN/m <sup>2</sup> ]	100.0
				$\nu$	–	0.25
				$m$	–	0.95
				$\sigma_L$	[kN/m <sup>2</sup> ]	10.0
				barotropy	–	$p$
				$E_0^{ref}$	[kN/m <sup>2</sup> ]	180000

3	sandy silt	HS-Brick			$\gamma_{0.7}$	–	0.0001
				Unit weight	$\gamma$	[kN/m <sup>3</sup> ]	18
				Non-linear	$\phi$	[°]	24
					$\psi$	[°]	0
					$c$	[kN/m <sup>2</sup> ]	5
					$E_{50}^{\text{ref}}$	[kN/m <sup>2</sup> ]	7200
					$R_f$	–	0.9
					$D$	–	0.25
			Stress history	$OCR$	–		1.0
				$K_0^{\text{NC}}$	–		0.59
				$p_{c0}^{\text{min}}$	[kN/m <sup>2</sup> ]		10.0
			Initial $K_0$ state	$K_0$	–		Automatic
			Elastic	$E_{\text{ur}}^{\text{ref}}$	[kN/m <sup>2</sup> ]		100000
				$\sigma_{\text{ref}}$	[kN/m <sup>2</sup> ]		100.0
				$\nu$	–		0.25
				$m$	–		0.80
				$\sigma_L$	[kN/m <sup>2</sup> ]		10.0
				barotropy	–		$p$
				$E_0^{\text{ref}}$	[kN/m <sup>2</sup> ]		300000
				$\gamma_{0.7}$	–		0.0002
			Unit weight	$\gamma$	[kN/m <sup>3</sup> ]		20
			Non-linear	$\phi$	[°]		32
				$\psi$	[°]		0
				$c$	[kN/m <sup>2</sup> ]		5
				$E_{50}^{\text{ref}}$	[kN/m <sup>2</sup> ]		35000
				$R_f$	–		0.9
				$D$	–		0.25
			Stress history	$q^{\text{POP}}$	[kN/m <sup>2</sup> ]		600
				$K_0^{\text{NC}}$	–		0.47
				$p_{c0}^{\text{min}}$	[kN/m <sup>2</sup> ]		10.0
			Initial $K_0$ state	$K_0$	–		Automatic

Table 4.6: Material properties of piles and foundation raft

Material	Model	Data group	Parameter	Unit	Value
Piles	Linear-elastic	Elastic	$E$	[MPa]	30000
			$\nu$	–	0.2
		Unit weight	$\gamma$	[kN/m <sup>3</sup> ]	24/5
Raft	Linear-elastic	Elastic	$E$	[MPa]	30000
			$\nu$	–	0.2
		Unit weight	$\gamma$	[kN/m <sup>3</sup> ]	25

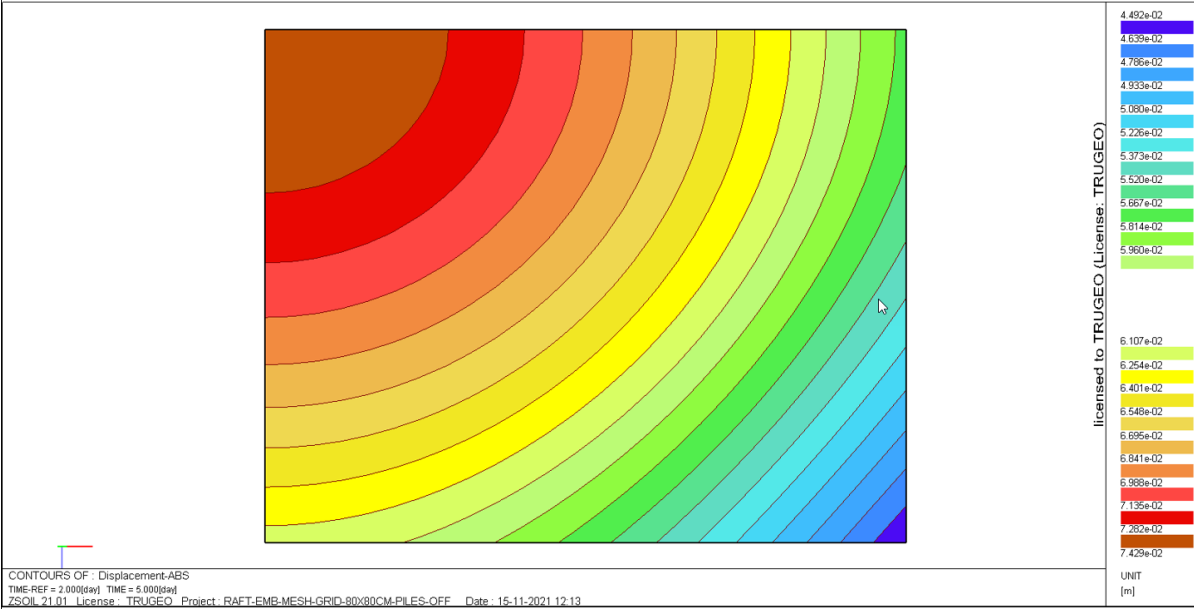


Figure 4.48: Settlements of the raft without piles at  $q = 150 \text{ kN/m}^2$  (grid size 80cm)

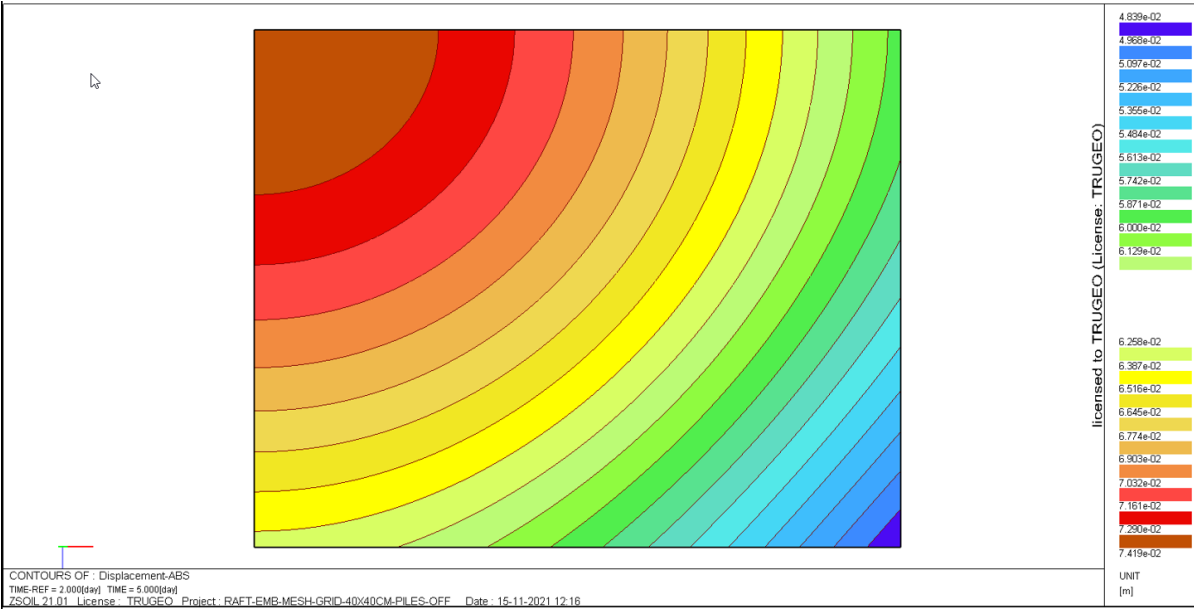


Figure 4.49: Settlements of the raft without piles at  $q = 150 \text{ kN/m}^2$  (grid size 40cm)

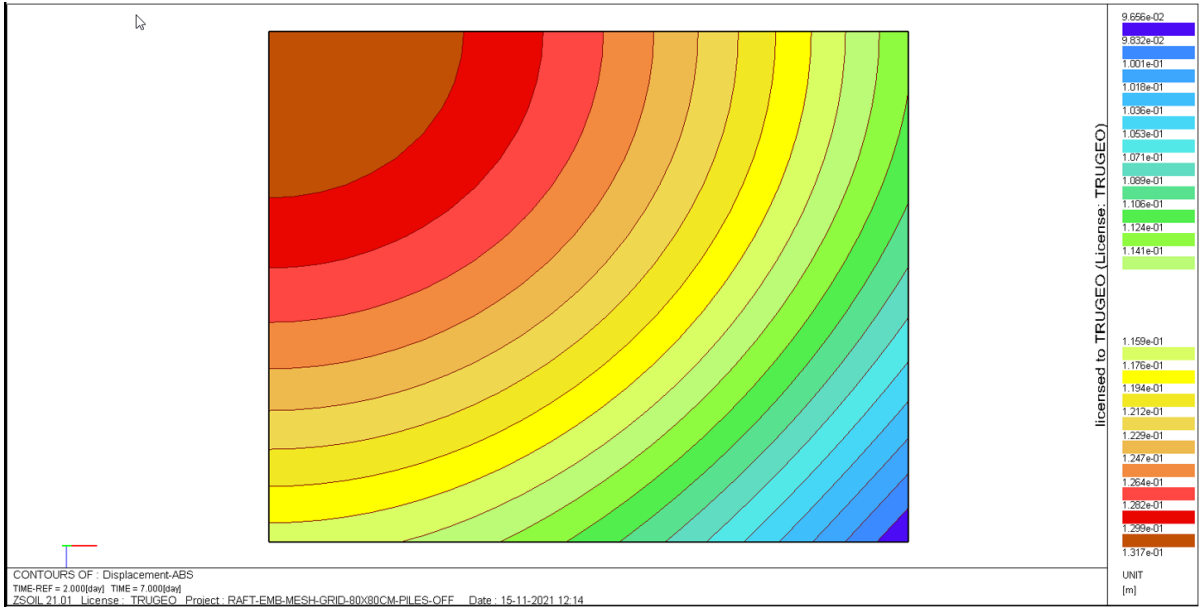


Figure 4.50: Settlements of the raft without piles at  $q = 300 \text{ kN/m}^2$  (grid size 80cm)

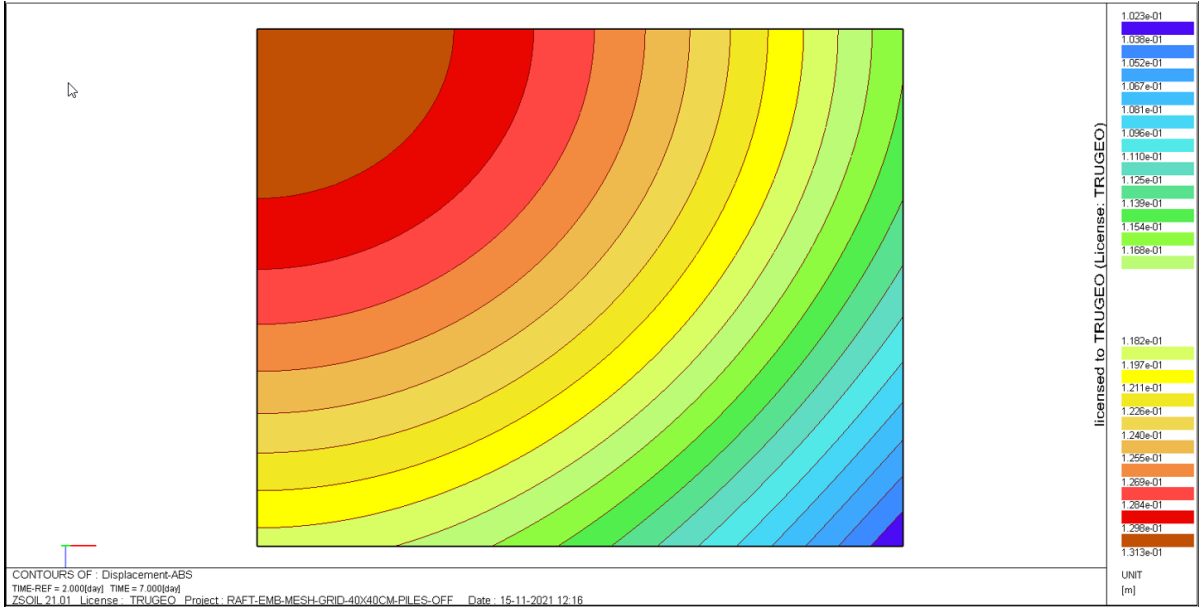


Figure 4.51: Settlements of the raft without piles at  $q = 300 \text{ kN/m}^2$  (grid size 40cm)

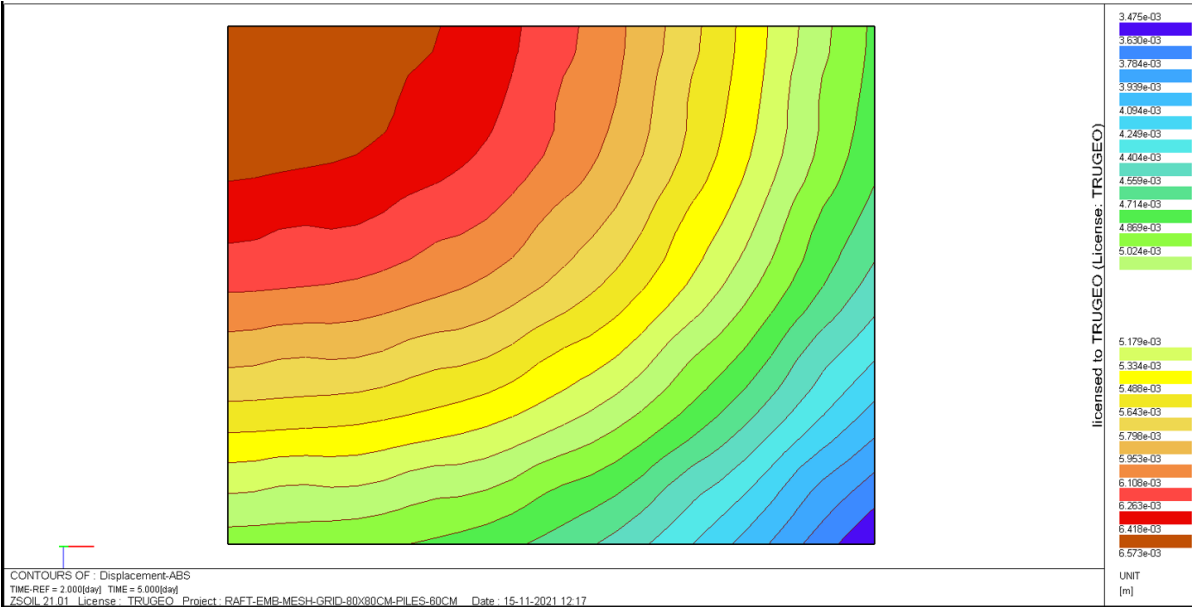


Figure 4.52: Settlements of the raft with piles at  $q = 150 \text{ kN/m}^2$  (grid size 80cm)

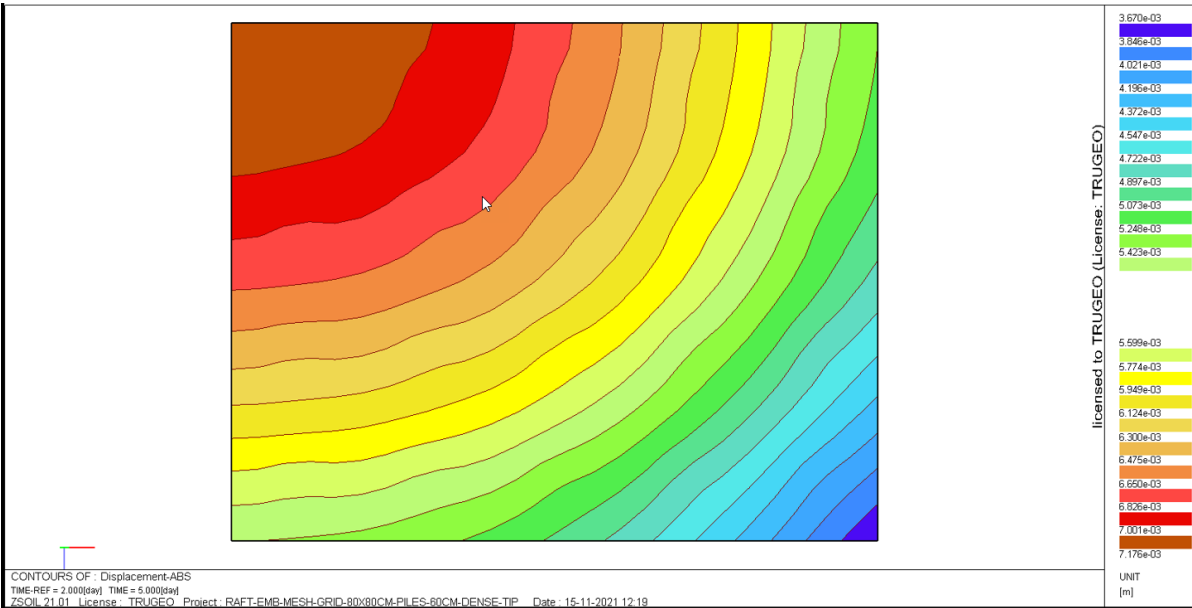


Figure 4.53: Settlements of the raft with piles at  $q = 150 \text{ kN/m}^2$  (grid size 80cm, dense piles tip zone)



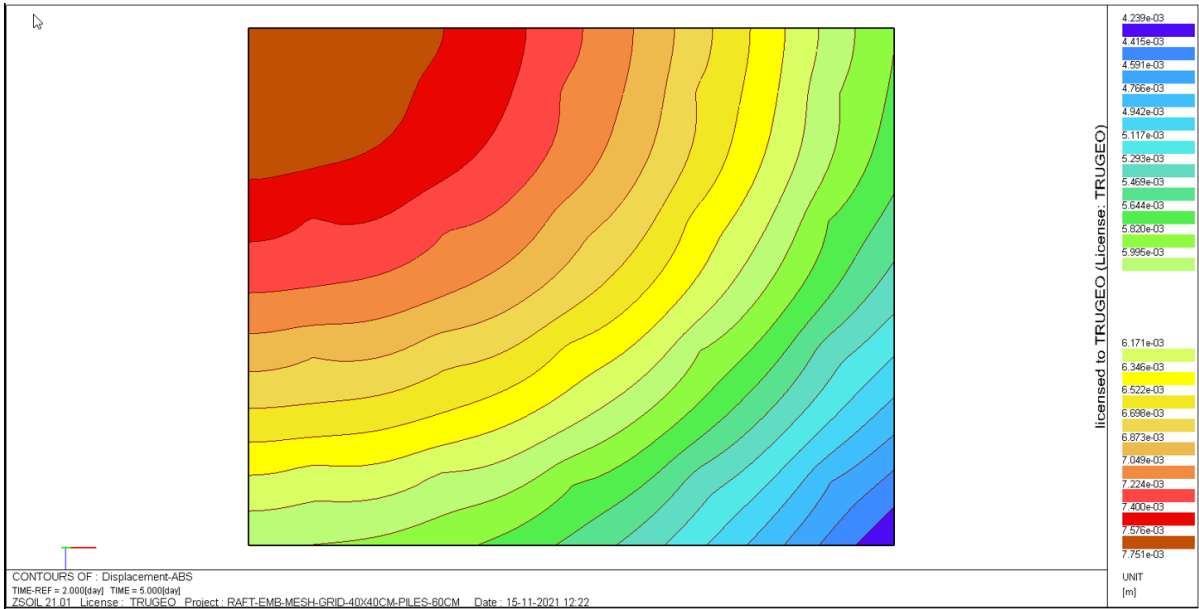


Figure 4.54: Settlements of the raft with piles at  $q = 150 \text{ kN/m}^2$  (grid size 40cm)

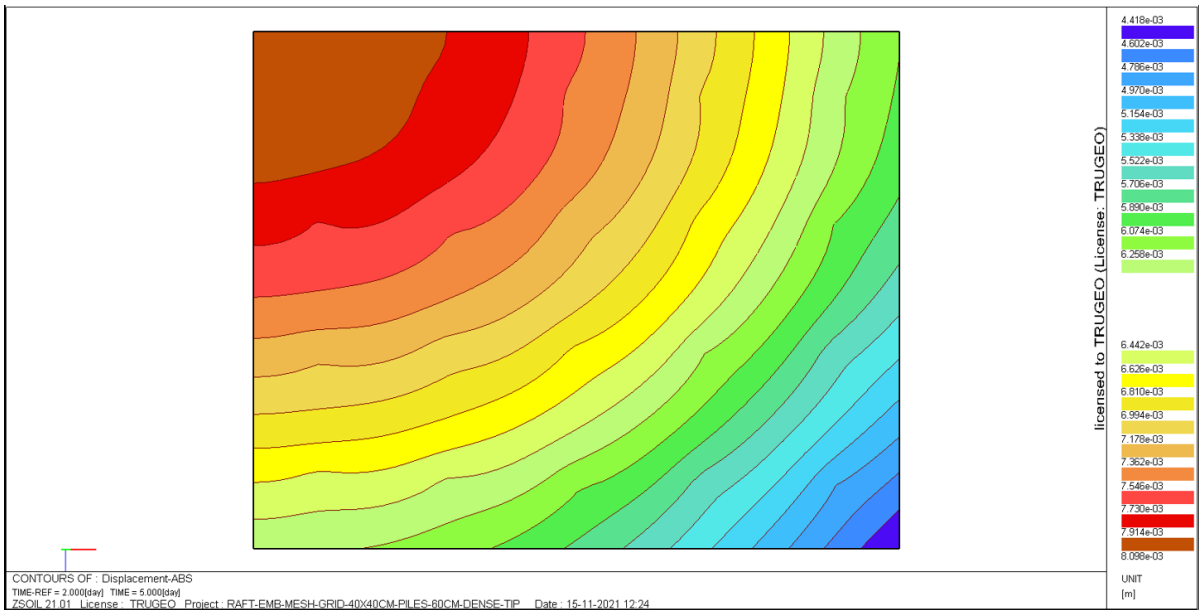


Figure 4.55: Settlements of the raft with piles at  $q = 150 \text{ kN/m}^2$  (grid size 40cm, dense piles tip zone)

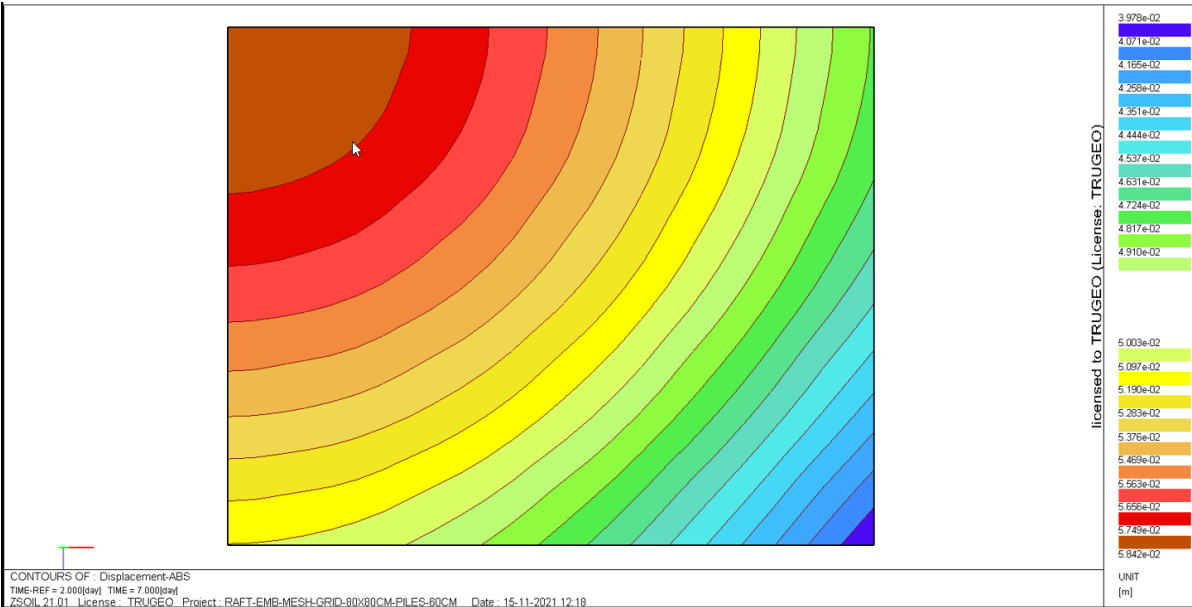


Figure 4.56: Settlements of the raft with piles at  $q = 300 \text{ kN/m}^2$  (grid size 80cm)

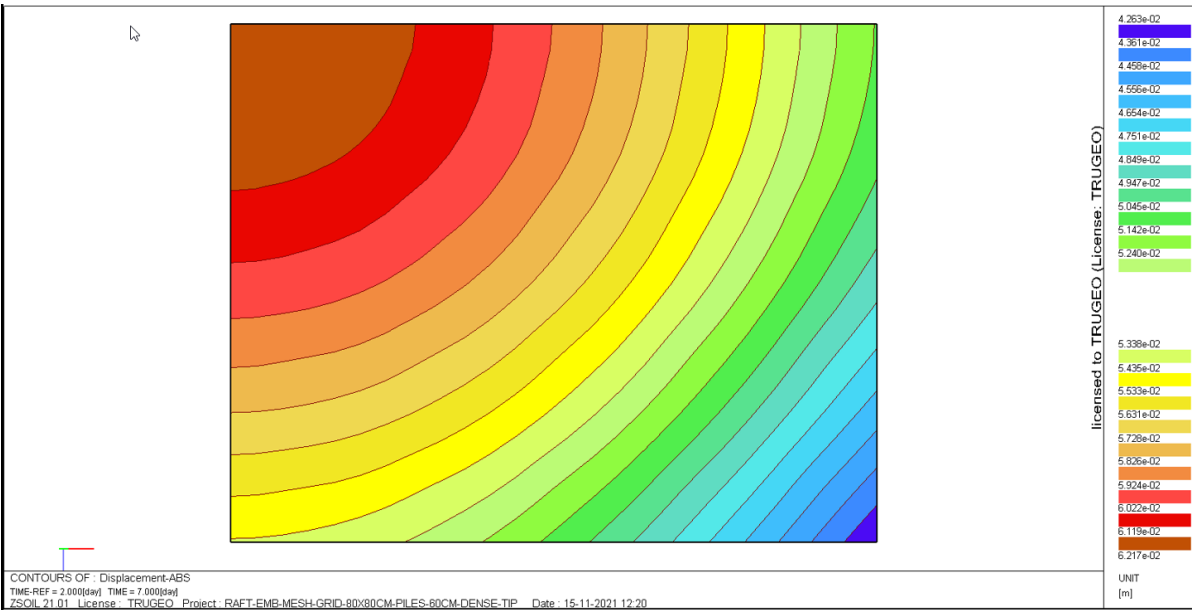


Figure 4.57: Settlements of the raft with piles at  $q = 300 \text{ kN/m}^2$  (grid size 80cm, dense piles tip zone)

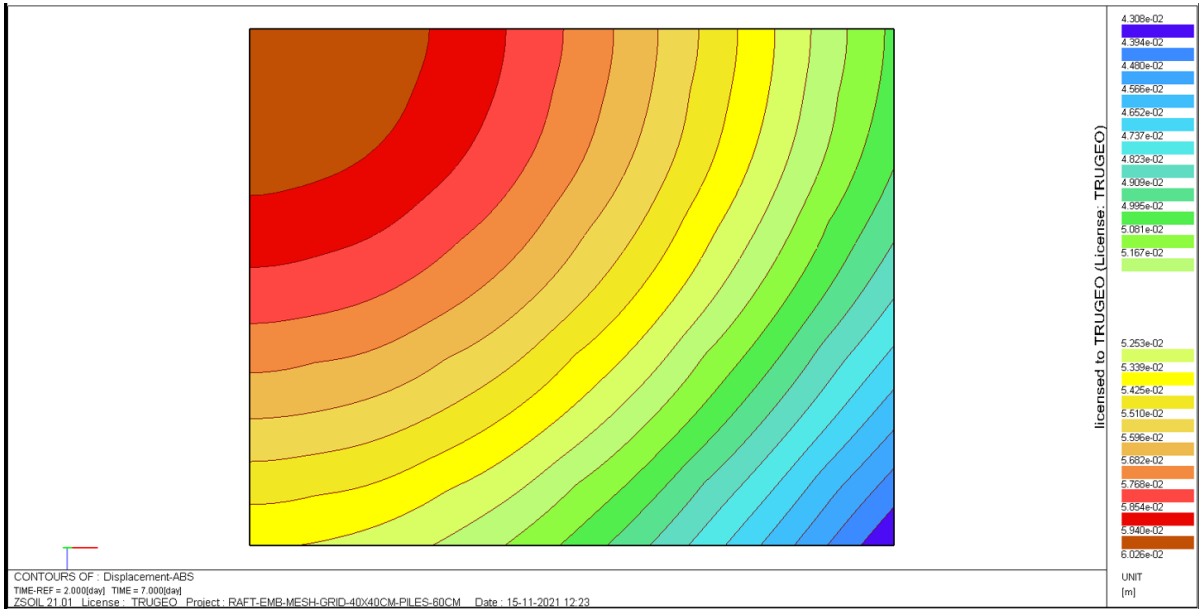


Figure 4.58: Settlements of the raft with piles at  $q = 300 \text{ kN/m}^2$  (grid size 40cm)

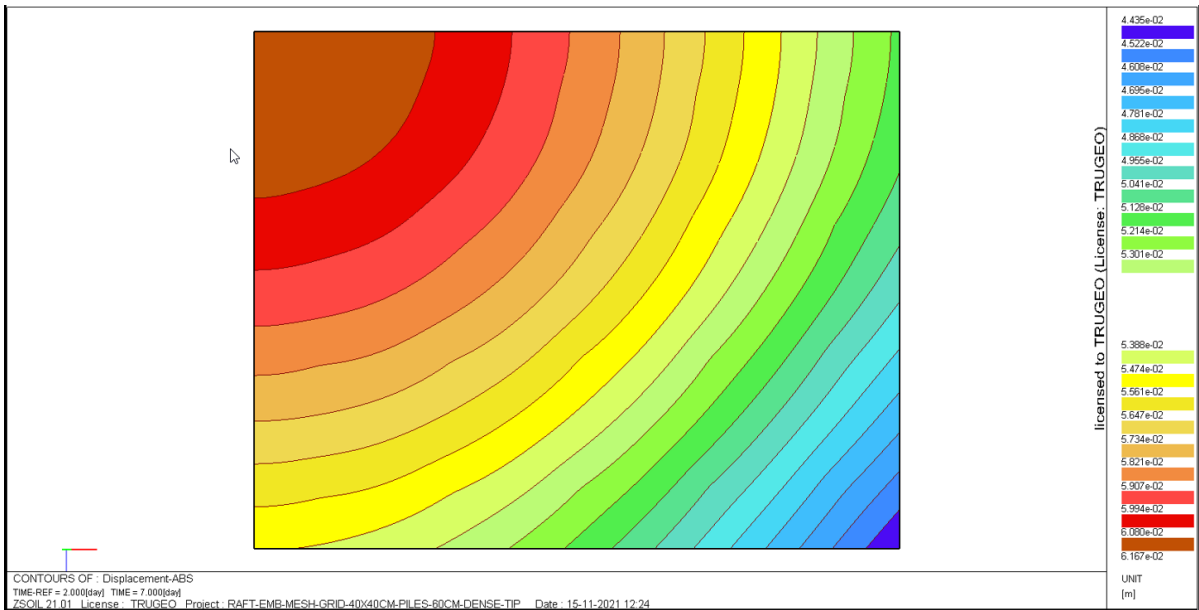


Figure 4.59: Settlements of the raft with piles at  $q = 300 \text{ kN/m}^2$  (grid size 40cm, dense piles tip zone)

Table 4.7: Comparizon of settlements

Mesh	Max. settl.	Min.settl.	Max.settl.	Min.settl.
	[mm]	[mm]	[mm]	[mm]
	q=150 kN/m <sup>2</sup>	q=150 kN/m <sup>2</sup>	q=300 kN/m <sup>2</sup>	q=300 kN/m <sup>2</sup>
80x80 (piles off)	45	74	97	132
40x40 (piles off)	48	74	102	132
80x80	4	7	40	58
80x80 (dense tip zone)	4	7	42	62
40x40	4	8	43	60
40x40 (dense tip zone)	4	8	44	62